공학석사 학위논문

First-principles study on the reaction mechanism in metal-air batteries

제일 원리 계산을 이용한 금속 공기 전지의 반응 메커니즘에 대한 연구

2014 년 2 월

서울대학교 대학원
재료공학부
이 병 주

First-principles study on the reaction mechanism in metal-air batteries

제일 원리 계산을 이용한 금속 공기 전지의 반응 메커니즘에 대한 연구

지도 교수 강 기 석

이 논문을 공학석사 학위논문으로 제출함

2014 년 2월

서울대학교 대학원

재료공학부

이 병 주

이 병 주의 석사 학위논문을 인준함

2014 년 2 월

위 원 장	박 병 우	(인)
부위원장	강 기 석	(인)
위 원	한 승 우	(인)

Abstract

First-principles study on the reaction mechanism in metal-air batteries

Lee, Byungju

Department of Material Science and Engineering

College of Engineering

The Graduate School

Seoul National University

Li/O_2 battery has the highest theoretical energy density among any battery systems reported to date. However, its poor cycle life and unacceptable energy efficiency from a high charging overpotential have been major limitations. Recently, much higher energy efficiency with low overpotential was reported for a new metal/oxygen system, Na/O_2 battery. This finding was unexpected since the general battery mechanism of the Na/O_2 system was assumed to be analogous to that of the Li/O_2 cell. Furthermore, it implies that fundamentally different kinetics are at work in the two systems. Here, we investigated the reaction mechanisms in the Na/O_2 cell using first-principles calculations. In comparative study with the Li/O_2 cell, we constructed the phase stability maps of the reaction products of Na/O_2 and Li/O_2 batteries based on the oxygen partial pressure, which explained why certain phases should be the main discharge products under different operating conditions. From surface calculations of NaO_2, Na_2O_2, and Li_2O_2 during the oxygen evolution reaction, we also found that the energy barrier for the NaO_2 decomposition was substantially lower than that of Li_2O_2 decomposition on major surfaces providing a hint for low charging overpotential of Na/O_2 battery.

Keywords: metal oxygen battery; sodium oxygen battery; first principles; polarization; overpotential, oxygen evolution reaction

Student Number: 2012-20622

Abstract ……..…….. i

Contents ……..……...iii

List of Tables …….…….. v

List of Figures …….vi

Chapter 1 Introduction……...…1

1.1 Motivation and outline…….…1

Chapter 2 Reaserch backgrounds…….....3

2.1. Introduction to metal/oxygen batteries...……...3

2.2. Introduction to first principles calculations……...5

Chapter 3 Computational methodology……...……...……..9

3.1. Computational details…… ……9

3.2. Surface energy calculations.....9

3.3. The phase stability calculations……...11

3.4. The oxygen evolution reaction…….12

3.5. The oxygen gas reference…….12

Chapter 4 Results and discussion…….……14

4.1. The bulk structures of discharge products …..……...……..…14

4.2. The phase stability map …….…….…16

4.3. The surface energies ……..…19

4.3.1. Terminations of the surface ...……...19

4.3.2. Wulff construction and equilibrium morphology …....…28

4.4. The oxygen evolution reaction mechanism ….……....32

4.5. Electronic conductivity of discharge product ……..……...40

Chapter 5 Conclusion……...……42

Reference

List of Tables

Table 1. Surface energies of pyrite NaO_2 for all possible terminations. The star symbols (*) indicate stoichiometric surfaces. The most stable termination of each surface was used to construct the Wulff shape. (in meV/Å ^{2})

Table 2. Surface energies of NaO_2 for all possible terminations. The star symbols (*) indicate stoichiometric surfaces. (in meV/Å ^{2})

Table 3. Surface energies of Na_2O_2 for all possible terminations. The star symbols (*) indicate stoichiometric surfaces. (in meV/Å ^{2})

Table 4. Surface energies of Li_2O_2 for all possible terminations. The star symbols (*) indicate stoichiometric surfaces. (in meV/Å ^{2}) The energies of terminations were in good agreement with the results of Mo *et al.*; [Reference 13 in the paper] slight differences derive from computational details. Note that Mo *et al.* referred to the $(11\bar{2}0)$ surface as $(1\bar{1}00)$, $(1\bar{1}00)$ as $(11\bar{2}0)$, $(11\bar{2}1)$ as $(1\bar{1}01)$, and $(1\bar{1}01)$ as $(11\bar{2}1)$. There are no stoichiometric terminations in the $(1\bar{1}01)$ and $(11\bar{2}1)$ surfaces, but Mo *et al.* considered stoichiometric terminations, resulting in different surface energies, for the $(1\bar{1}01)$ and $(11\bar{2}1)$ surfaces.

Table 5. Calculated surface energies of the low-index surfaces of pyrite NaO_2, marcasite NaO_2, Na_2O_2, and Li_2O_2 under the most oxidizing and reducing conditions (in meV/Å ^{2}).

List of Figures

Scheme 1. Schematic drawing of the Li/air battery system.

Figure 1. Bulk structures of (a) marcasite NaO_2, (b) pyrite NaO_2, (c) Na_2O_2, and (d) Li_2O_2. Green, yellow, and red atoms correspond to sodium, lithium, and oxygen, respectively. Dotted lines indicate the oxygen dumbbells in the structure.

Figure 2. Phase stability map of various lithium/sodium oxides as a function of oxygen chemical potential or oxygen partial pressure. The red line is the oxygen chemical potential where oxygen dissolved in electrolyte is in equilibrium with 1 atm oxygen gas. The blue region is the oxygen chemical potential range under non-equilibrium conditions that can result from fast consumption of O_2 in the electrolyte during discharge.

Figure 3. Surface unit cells of pyrite NaO_2. The yellow and red atoms correspond to sodium and oxygen, respectively. Three low-index surfaces were considered. As termination with an O atom rather than an O_2 dumbbell made the surface unstable, such terminations were not considered in this study.

Figure 4. Surface unit cells of marcasite NaO_2. The yellow and red atoms correspond to sodium and oxygen, respectively. Seven low-index surfaces were considered.

Figure 5. Surface unit cells of Na_2O_2. The yellow and red atoms correspond to sodium and oxygen, respectively. Five low-index surfaces were considered. There were many terminations because of the low symmetry of the Na_2O_2 structure. The top and bottom surfaces of the $(11\bar{2}0)$ and $(11\bar{2}1)$ surfaces could not be terminated equally because of low symmetry, hence atoms that were positioned at the same crystallographic site were terminated.

Figure 6. Surface unit cells of Li_2O_2. The green and red atoms correspond to lithium and oxygen, respectively. Five low-index surfaces were considered.

Figure 7. Wulff shapes of (a), (b) pyrite NaO_2, (d), (e) marcasite NaO_2, (f), (g) Na_2O_2, and (h), (i) Li_2O_2 during the OER on the corresponding surfaces. The left sides (a), (d), and (f) are for the most oxidizing conditions, and the right sides (b), (e), and (g) are for the most reducing conditions of each material. (c) SEM image of the pyrite NaO_2 crystallite in the discharged Na/O_2 cell. The calculated energy barrier of OER for all the surfaces are represented as a colored map in the Wulff shape of each material. Major surfaces of the Na discharge products are comprised of the surfaces with low OER barriers. Reproduced with permission from Ref. 14. Copyright 2013 Nature Publishing Group.

Figure 8. OER energy profile of the surfaces in pyrite NaO_2, marcasite NaO_2, Na_2O_2, and Li_2O_2. The surfaces of interest were selected: (a) (110) surface of pyrite NaO_2, (b) (100) surface of pyrite NaO_2, (c) (101) surface of marcasite NaO_2, (d) (010) surface of marcasite NaO_2, (e) (0001) surface of Na_2O_2, (f) $(1\bar{1}00)$ surface of Na_2O_2, (g) (0001) surface of Li_2O_2, and (h) $(1\bar{1}00)$ surface of Li_2O_2. The most favorable reaction paths are shown. The chemical steps are shown in red.

Figure 9. The OER energy profile for pyrite NaO_2. (a) (100) surface of pyrite NaO_2, (b) (110) surface of pyrite NaO_2, (c) (111) surface of pyrite NaO_2. The most favorable reaction paths are shown. The chemical steps are shown in red.

Figure 10. The OER energy profile for marcasite NaO_2. (a) (001) surface of marcasite NaO_2, (b) (010) surface of marcasite NaO_2, (c) (011) surface of marcasite NaO_2, (d) (100) surface of marcasite NaO_2, (e) (101) surface of marcasite NaO_2, (f) (110) surface of marcasite NaO_2, and (g) (111) surface of marcasite NaO_2. The most favorable reaction paths are shown. The chemical steps are shown in red.

Figure 11. The OER energy profile for Na_2O_2. (a) The (0001) surface of Na_2O_2, (b) the $(1\bar{1}00)$ surface of Na_2O_2, (c) the $(11\bar{2}0)$ surface of Na_2O_2, (d) the $(1\bar{1}01)$ surface of Na_2O_2, and (e) the $(11\bar{2}1)$ surface of Na_2O_2. The most favorable reaction paths are shown. The chemical steps are shown in red.

Figure 12. The OER energy profile for Li_2O_2. (a) (0001) surface of Li_2O_2, (b) $(1\bar{1}00)$ surface of Li_2O_2, and (c) $(11\bar{2}1)$ surface of Li_2O_2. The most favorable reaction paths are shown. The chemical steps are shown in red. Since $(11\bar{2}0)$ and $(1\bar{1}01)$ surfaces cannot be found in Wulff shape, the OER profiles of these surfaces were not calculated.

Figure 13. Density of state of (a) pyrite NaO_2, (b) marcasite NaO_2, (c) Na_2O_2, (d) Li_2O_2.

Chapter 1. Introduction

1.1 Motivation and outline

With the high demand for large-scale energy storage devices, it is increasingly important to develop new battery systems with higher energy densities and lower costs. Metal/oxygen batteries are promising new candidates for such applications. Compared with conventional Li-ion batteries (LIBs), metal/oxygen batteries can provide exceptionally higher theoretical energy densities without a use of transition metal element in its reaction. Li/O_2 battery,[1-5] one of the most extensively studied metal/oxygen systems, can deliver the energy which is ~10 times higher than those of state-of-art LIBs. However, despite this advantage, Li/O_2 batteries have suffered from poor rechargeability and low energy efficiency due to a high polarization during charging (~60%).[2, 5-8] The highest efficiency achieved using a nanoporous gold current collector was 70%,[9] indicating that 30% of the unused energy was lost in every cycle. Recently, Hartmann *et al.*[10] reported a new metal/oxygen system based on Na, which was analogous to the Li/O_2 system in terms of the cell construction and the expected operating mechanism.[10-13] One of the most surprising aspects of the Na/O_2 cell was that the polarization was extremely low, enabling an energy efficiency of around 90%, even in the absence of a catalyst. Moreover, it could be operated with the micron size of the discharge products. This is in marked contrast with the Li/O_2 system and implies that fundamentally different kinetics are at work in the two systems.

In the present study, we investigate the reaction mechanism in the Na/O_2 cell using first-principles calculations. In this approach, the phase stability maps of discharge products are constructed for reactions in Na/O_2 and Li/O_2 batteries as a function of oxygen partial pressures. From the calculation of the surface structures of these discharge products, we also estimate the energy barriers for the oxygen evolution reaction (OER) on the major surfaces. In comparison with the results of Li/O_2 cell, we discuss on the possible origin of low overpotential of Na/O_2 cell. This fundamental study on the

reaction mechanism is believed to provide insights on the distinct reactions in various metal/oxygen batteries.

Chapter 2. Research backgrounds

2.1. Introduction to metal/oxygen batteries

Metal oxygen batteries have shown great promise as alternative post-LIB (Li-ion battery) energy storage systems because of their exceptionally high energy densities, which are ~10 times higher than those of state-of-the-art LIBs. This is because metal ion directly reacts with oxygen gas, without involvement of heavy transition metal ion in the reaction. Li/O_2 battery, one of the most extensively studied metal/oxygen systems, are suggested as a next generation battery type for electrical vehicle (EV) and hybrid electrical vehicle (HEV) because of its exceptionally high energy density up to ~3000Wh kg^{-1}.

Simple schematic of Li/O_2 battery system is shown in Scheme 1. The lithium anode is in contact with the electrolyte and forms a SEI (solid electrolyte interface) layer. This protects further reaction between lithium metal and electrolyte. In cathode side, there are only current collector, usually porous carbon, providing the site for charge/discharge reaction. The non-aqueous electrolyte is used to hinder contamination of lithium metal anode. During the discharge, spontaneous reaction occurs :

$$2Li + O_2 \rightarrow Li_2O_2$$

equilibrium of which is 2.96 V. In case of charging, the decomposition reaction of Li_2O_2 occurs with extremely high overpotential. Although their implementation holds the greatest promise in a number of applications ranging from portable electronics to electric vehicles, there are also impressive challenges in development of cathode materials and electrolyte systems of these batteries.

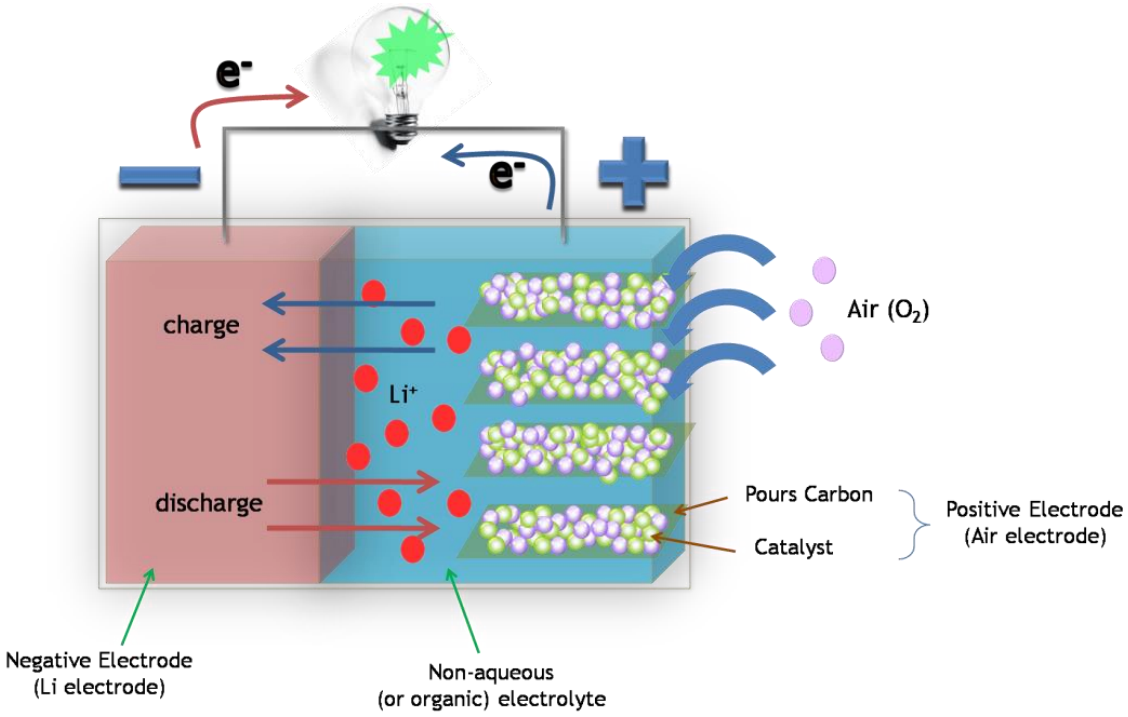

Scheme 1. Schematic drawing of the Li/air battery system.

2.2. Introduction to first principles calculation

First principles calculations (or *ab initio* in Latin, which means 'from the beginning') is the simulation method that start directly at the level of established laws of physics, which need no initial parameters. Different from all other calculation methods, first principles calculations require parameters which are parameterized to experiments or quantum mechanical calculations. First principles calculation only requires nuclear charges and numbers of electrons as input information without any empirical model and fitting parameters.

In first principle calculation, wave function of materials which contains all the information of a given system is calculated by solving time-dependent Schrödinger equation. Time-independent Schrödinger equation is as follows:

$$H\Psi = E\Psi$$

where H is Hamiltonian operator, Ψ is the wave function, and E is the total energy of the system. The Hamiltonian operator H can be expressed as follows:

$$H = -\sum_{i=1}^{N}\frac{1}{2}\nabla_i^2 - \sum_{i=1}^{M}\frac{1}{2M_A}\nabla_A^2 - \sum_{i=1}^{N}\sum_{A=1}^{M}\frac{Z_A}{r_{iA}} + \sum_{i=1}^{N}\sum_{j>i}^{N}\frac{1}{r_{ij}} + \sum_{A=1}^{M}\sum_{B>A}^{M}\frac{Z_A Z_B}{R_{AB}}$$

The first and second terms are kinetic operators of electrons and nuclei, respectively. The third, fourth, and fifth terms account the interaction of nuclei-electrons, electrons-electrons, and nuclei-nuclei, respectively.

In multi atom system, the third, fourth, and fifth terms of H are insoluble because we cannot determine the position of each nuclei and electrons. Therefore, Schrödinger equation cannot be solved in this situation. Hence some approximations are introduced to solve the problem. According to the Born-Oppenheimer approximation, the motions of nuclei are negligible compared to those of electrons because the mass of nuclear is over 1000 times heavier than electron. Hence, the kinetic energies of nuclei can be neglected and the Coulomb interaction term between the nuclei can be treated as constant. In this situation, we can express the Hamiltonian operator as sum of nuclear Hamiltonian and electronic Hamiltonian. Therefore, we can calculate

wave function of electrons by solving the Schrödinger equation involving just electron Hamiltonian operator as follows:

$$H_{electron} = \sum_i \frac{1}{2}\nabla_i^2 - \sum_i \sum_A \frac{Z_A}{r_{iA}} + \sum_i \sum_{j>i} \frac{1}{r_{ij}}$$

The energy of system, that is the eigenvalue of Schrödinger equation, can be obtained as a result.

$$E_{total} = E_{electron} + \sum_A \sum_{B>A} \frac{Z_A Z_B}{R_{AB}}$$

The nuclei Schrödinger equation remained can be solved with the kinetic operation of nuclei and the total energy. We should consider the spin state of electrons to describe the properties of materials proper. Therefore, spin functions α(ω) and β(ω) were regarded into the wave function. In order to satisfy Pauli Exclusion Principles for electrons, Slater determinants were used for the wave function.

However, we still cannot solve electronic Hamiltonian because electron-electron interactions were not determined in N-electron system. Therefore Hartree-Fock method approximates that certain electron interacts with the potential field which was formed by other electrons. With this approximation, the system can be expressed by one-electron Schrödinger equation and this can be solved with the variational method, which means that complicated N-body problem can be converted to one-body problem.

A different approach to solving time-independent Schrödinger equations, density functional theory (DFT), was suggested because of large computational cost of Hartree-Fock type calculation. DFT calculations suggest two concepts; "All properties of all states are formally determined by the ground state density" and "The ground state energy of the system is a functional to the ground state density" as Hohenberg-Kohn theorem. Therefore, DFT only calculates the 3 coordinate electron density compared to the 4N coordinate electron wave function in Hartree-Fock method. . The ground state energy can be expressed as follows:

$$\mathrm{E}[\rho] = \mathrm{T}[\rho] + V_{ee}[\rho] + \int \rho(\vec{r})\, V_{Ne}(\vec{r})\, \mathrm{d}\,\vec{r}$$

where ρ is density, each term represents kinetic energy, electron-electron interaction, and Coulomb potential between electron and nuclei. The first and second terms are called as universal functional, F[ρ]. This F[ρ] term is key factor for correct solution. However, the correct universal functional is unknown, so Kohn and Sham suggested the approximated form of F[ρ] as follows:

$$F[\rho] = T_s[\rho] + J[\rho] + E_{xc}[\rho]$$

where $T_s[\rho]$ is the kinetic energy of non-interacting electrons and the Hartree term J[ρ] is a classical Coulomb repulsion. $E_{xc}[\rho]$ term is exchange-correlation energy of electrons includes the difference in kinetic energies between non-interacting electrons and real electrons as well as J[ρ] arising from the correlations between electrons.

There are some approximations for $E_{xc}[\rho]$ term because it is still unknown term. Kohn and Sham suggested the local density approximation (LDA) which is most common approximations to exchange-correlation energy:

$$E_{xc} = \int \rho(\vec{r})\varepsilon_{xc}(\rho)\mathrm{d}\vec{r}$$

Where ε_{xc} is the exchange-correlation energy per electron for a uniform electron gas. However, electron density of materials are non-uniform in battery materials like transition metal oxide. Thus the Generalized Gradient Approxmiation (GGA) is usually chosen because it can treat the non-local electron density system by the consideration of the gradient of the electron density.

In this paper, first principles calculations were performed on the basis of the spin-polarized DFT using a GGA within the Perdew-Burke-Ernzerhof (PBE) functional. A plane-wave basis set and the projector-augmented wave (PAW) method as implemented in the Vienna *ab initio* simulation package (VASP) were used.[14] The incomplete cancelation of the self-interaction of GGA or LDA is often reported to result in large errors especially for systems with strong localization of the metal *d* orbitals, such as transition metal polyoxianion materials.[15, 16]

Chapter 3. Computational methodology

3.1. Computational details

First-principles calculations were conducted to determine the energies of given states of materials, based on the spin-polarized generalized gradient approximation (GGA) using density functional theory (DFT). Perdew-Burke-Ernzerhof exchange-correlation parameterization was used. We performed the calculations with the Vienna *ab initio* simulation package (VASP)[14] using the projector-augmented wave (PAW)[17] method. PAW potentials have shown good predictive capability in battery materials.[15, 16, 18-21] A plane-wave basis with an energy cutoff of 500 eV was used, and appropriate *k*-point meshes were chosen to ensure that the total energies converged within 1 meV per formula unit. All structures were fully relaxed. For surface energy calculations, we adopted a slab/vacuum geometry composed of repeating slabs and vacuum layers.[20-26] A convergence test of the vacuum and slab thicknesses indicated that a vacuum thickness of 10 Å and slab thickness > 20 Å were sufficient for convergence within 1 meV/Å^2 for the surface energies.

3.2. Surface energy calculations

The free energy of a surface was calculated by equation (1):

$$\gamma = \frac{1}{2A}[G_{slab} - N_O {\mu_O}^{bulk} - N_M {\mu_M}^{bulk}] \quad (1)$$

where G_{slab} is the total free energy of the slab supercell, A is the area of the exposed surface, N_O and N_M are the numbers of oxygen and metal atoms in the slab, respectively, and ${\mu_O}^{bulk}$ and

$\mu_M{}^{bulk}$ are the chemical potentials of oxygen and metal in their bulk phases, respectively. *M* represents lithium or sodium. Atoms that were positioned at the same crystallographic sites were terminated equally from the top and bottom surfaces to make the two terminations identical; hence, a factor of 1/2 was considered for the two surfaces. The chemical potential of oxygen, $\mu_O{}^{bulk}$, can be expressed in terms of $\mu_M{}^{bulk}$ as follows:

$$\mu_O{}^{Li_2O_2} = \frac{1}{2}G^{Li_2O_2} - \mu_{Li}{}^{Li_2O_2} \quad (2)$$

$$\mu_O{}^{Na_2O_2} = \frac{1}{2}G^{Na_2O_2} - \mu_{Na}{}^{Na_2O_2} \quad (3)$$

$$\mu_O{}^{NaO_2} = \frac{1}{2}G^{NaO_2} - \frac{1}{2}\mu_{Na}{}^{NaO_2} \quad (4)$$

By combining equations (2), (3), and (4) with equation (1), the surface energies of Li_2O_2, Na_2O_2, and NaO_2 can be rewritten as:

$$\gamma_{Li_2O_2} = \frac{1}{2A}[G_{slab} - \frac{1}{2}N_O \cdot G^{Li_2O_2} - (N_{Li} - N_O) \cdot \mu_{Li}{}^{Li_2O_2}] \quad (5)$$

$$\gamma_{Na_2O_2} = \frac{1}{2A}[G_{slab} - \frac{1}{2}N_O \cdot G^{Na_2O_2} - (N_{Na} - N_O) \cdot \mu_{Na}{}^{Na_2O_2}] \quad (6)$$

$$\gamma_{NaO_2} = \frac{1}{2A}[G_{slab} - \frac{1}{2}N_O \cdot G^{NaO_2} - (N_{Na} - \frac{1}{2}N_O) \cdot \mu_{Na}{}^{NaO_2}] \quad (7)$$

The plausible range for chemical potentials of Li and Na can be determined by considering the two end members of the phases into which the target material transforms in either a reducing or oxidizing environment.[24, 25, 27] For example, Li_2O_2 can be reduced into Li_2O in a lithium-rich environment or oxidized into $Li_\delta O_2$ (δ ~0) in a lithium-deficient environment. The maximum and minimum of the plausible range of the lithium chemical potential are determined by the following reactions:

$$\mu_{Li}{}^{max,Li_2O_2} = G^{Li_2O} - \frac{1}{2}G^{Li_2O_2} \qquad \frac{1}{2}\,Li_2O_2 + Li \rightarrow Li_2O \quad (8)$$

$$\mu_{Li}{}^{min,Li_2O_2} = \frac{1}{2}G^{Li_2O_2} - \mu_O{}^0 \qquad \frac{1}{2}Li_2O_2 \rightarrow Li + \frac{1}{2}O_2 \quad (9)$$

where $G^{Li_2O_2}$ and G^{Li_2O} are the free energies per formula unit of Li_2O_2 and Li_2O, respectively, and $\mu_O{}^0$ is the chemical potential of oxygen gas at 298 K and 1 atm. Similarly, for Na_2O_2:

$$\mu_{Na}{}^{max,Na_2O_2} = G^{Na_2O} - \frac{1}{2}G^{Na_2O_2} \quad \frac{1}{2}\,Na_2O_2 + Na \rightarrow Na_2O \quad (10)$$

$$\mu_{Na}{}^{min,Na_2O_2} = G^{Na_2O_2} - G^{NaO_2} \qquad Na_2O_2 \rightarrow Na + NaO_2 \quad (11)$$

where G^{Na_2O}, $G^{Na_2O_2}$, and G^{NaO_2} are the free energies per formula unit of Na_2O, Na_2O_2, and NaO_2,

respectively. Unlike Li_2O_2, Na_2O_2 can be reduced to form the superoxide NaO_2; NaO_2 is stable under ambient conditions, while LiO_2 is thermodynamically unstable. Therefore, the free energy of the superoxide is considered in calculation of the minimum chemical potential of Na in Na_2O_2. Likewise, for NaO_2:

$$\mu_{Na}{}^{max,NaO_2} = G^{Na_2O_2} - G^{NaO_2} \qquad NaO_2 + Na \rightarrow Na_2O_2 \qquad (12)$$

$$\mu_{Na}{}^{min,NaO_2} = G^{NaO_2} - 2\mu_O{}^0 \qquad NaO_2 \rightarrow Na + O_2 \qquad (13)$$

3.3. The phase stability calculations

The phase stability maps of various metal oxides were constructed as a function of oxygen partial pressure as follows. From equations (10) and (11), the stability of the Na_2O_2 phase is found within the range of $\mu_{Na}{}^{min,Na_2O_2} \leq \mu_{Na} \leq \mu_{Na}{}^{max,Na_2O_2}$, which can be converted to the range of $\mu_O{}^{Na_2O_2}$ using equation (3). Similarly, the stability of other phases can be expressed as a function of the chemical potential of oxygen. A phase stability map was drawn from the maximum and minimum limits of the oxygen chemical potential at which the phase was stable. Using equation (14), the phase stability map can be redrawn as a function of oxygen partial pressure.

$$\mu_O(T,P) - \mu_O{}^0 = \frac{1}{2}RTln\left(P_{O_2}\right) \qquad (14)$$

The surface energy was calculated to estimate the equilibrium morphologies of discharge products. The energies of the seven low-index surfaces; (001), (010), (011), (100), (101), (110), and (111) were calculated for marcasite NaO_2 by the vacuum/slab model, while the energies of the three low-index surfaces; (100), (110), (111) were calculated for pyrite NaO_2 due to its higher symmetric space group. The energies of the five low-index surfaces; (0001), $(11\bar{2}0)$, $(1\bar{1}00)$, $(11\bar{2}1)$, and $(1\bar{1}01)$ were considered for both Na_2O_2 and Li_2O_2.

3.4. The oxygen evolution reaction

The reaction free energy of the intermediate steps was calculated as follows:

$$\Delta G^{slab} = \frac{1}{2}[E_{slab}^{step} - E_{slab}^{ini} - \Delta N_O \cdot \mu_O^0 - \Delta N_M \cdot (\mu_M^{metal} - eU)] \quad (15)$$

where E_{slab}^{step} is the free energy of the slab at each step, E_{slab}^{ini} is the initial free energy of the slab, ΔN_O and ΔN_M are the number of metal and oxygen atoms removed from the surface, and eU is electron energy under the charging potential. If there is no applied potential ($U = 0\ V$), then the entire energy step is uphill along the removal of atoms from the surface; therefore, the reaction is not spontaneous.

3.5. The oxygen gas reference

With regard to the oxygen chemical potential, ${\mu_O}^0$, it is known that the GGA calculation overestimates the binding energy of the oxygen double bond in oxygen gas.[28] Different oxygen references have been proposed for correcting overbinding,[20, 29-31] and there is as yet no consensus regarding the best reference correction. In the present study, the oxygen reference for the Li/O_2 cell was chosen from the formation energy of Li_2O_2 according to the reaction $2Li_2O + O_2 \rightarrow 2Li_2O_2$. In the case of the Na/$O_2$ cell, the oxygen reference value was considered from the reaction $2Na_2O + O_2 \rightarrow 2Na_2O_2$. However, the difference between the two values was below 0.06 eV per oxygen atom. This difference affected the surface energies at the O_2 limit (minimum μ_{Li} or μ_{Na} cases) by ~5 meV/Å^2, but it did not change the most stable termination or surface. Hence, the oxygen reference for lithium peroxide formation, ${\mu_O}^0 = -4.985$ eV,[20] was used in the entire calculation.

Chapter 4. Results and discussion

4.1. The bulk structures of discharge products

Figure 1 shows the crystal structures of marcasite NaO_2, pyrite NaO_2, Na_2O_2, and Li_2O_2. Although they have different oxygen stackings, the basic unit of each lattice contains the oxygen dumbbell. This is attributed to the strong oxygen-oxygen bond, which is commonly observed in alkali metal peroxides and superoxides.[32] The sodium ions in both NaO_2 phases occupy octahedral sites, whereas those in Na_2O_2 occupy prismatic sites. This is in contrast to Li_2O_2 where the lithium ions occupy both octahedral and prismatic sites in alternating layers. These various metal-oxygen bonding environments are expected to affect the surface properties and the OER mechanism, which will be discussed in detail later.

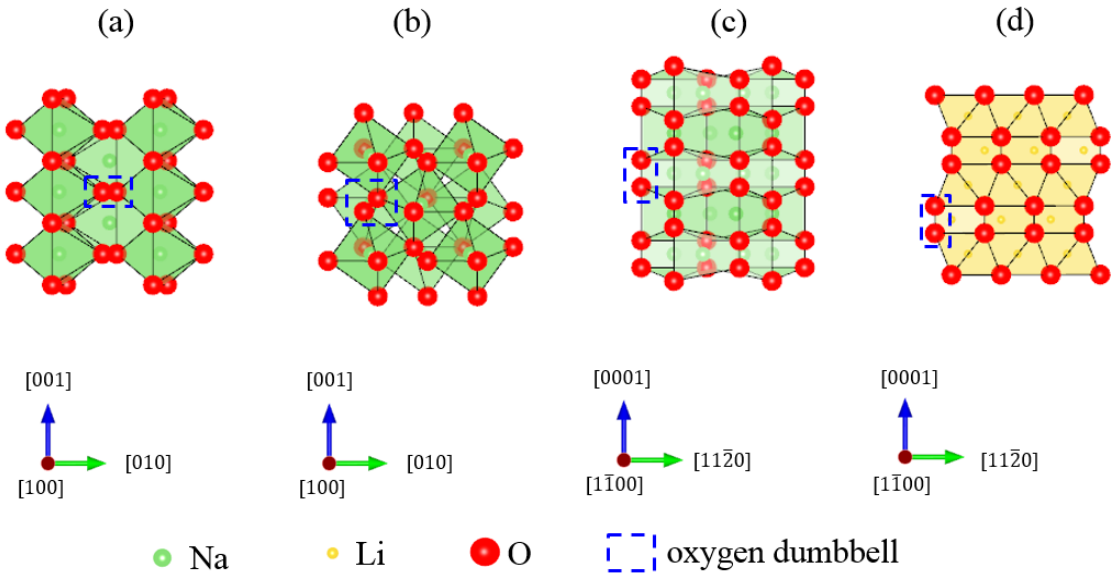

Figure 1. Bulk structures of (a) marcasite NaO_2, (b) pyrite NaO_2, (c) Na_2O_2, and (d) Li_2O_2. Green, yellow, and red atoms correspond to sodium, lithium, and oxygen, respectively. Dotted lines indicate the oxygen dumbbells in the structure.

4.2. The phase stability map

It has not yet been clarified what is the major discharge product for the Na/O_2 cell and under what conditions certain discharge products are formed. Hartmann *et al.*[10] observed pyrite NaO_2 as the discharge product, while Kim *et al.*[11] and Liu *et al.*[13] reported Na_2O_2 as the major product. Figure 2 shows that the stable discharge phase is determined by the oxygen partial pressure of the Na/O_2 cells in operation. In the figure, the stable sodium/lithium oxides phases are illustrated as a function of oxygen partial pressure. While the marcasite NaO_2 was found to be ground state structure at 0K from the calculation, the energy difference with that of pyrite phase was small, 40 meV/f.u., indicating the uncertainty on the room temperature phases in the electrochemical system. Thus, we plotted both phases of NaO_2 in the map. Marcasite and pyrite NaO_2 phases were found to be far more stable than Na_2O_2 phase when the μ_O is equal to that of the standard condition, $T = 298\,K$ and $P_{O_2} = 1\,atm$, as indicated by the red arrow in Figure 2. It shows that NaO_2 is likely the first discharge product in Na/O_2 reactions at the standard condition. Even under oxygen-deficient conditions, NaO_2 seemed to be stable up to P_{O_2} ~10^{-8} *atm*. It was found that Na_2O_2 phase is stable within range of $-0.67 \leq \mu_O - {\mu_O}^0 \leq -0.25$ eV or $-0.67 \leq \mu_O - {\mu_O}^0 \leq -0.21$ eV in comparison to marcasite and pyrite NaO_2 phases, respectively. On the other hand, Na_2O is stable only under extremely reducing conditions.

Using similar calculations for the Li/O_2 system, our results showed that Li_2O_2 was the most stable phase at ambient conditions, which was in good agreement with experimental observations.[2, 8] Li_2O was stable under mildly reducing conditions, suggesting that the formation of Li_2O is also possible energetically during Li/O_2 cell operation. On the other hand, the LiO_2 phase (ICSD # 642216) forms only at very high oxygen pressure, ~10^{98} *atm*, indicating that it is unlikely to be formed under the normal Li/O_2 cell operating conditions. Nevertheless, it should be noted that the actual environment in the cells may be significantly deviated from the equilibrium, resulting in the formation of kinetically favored phases. For example, in the typical operating conditions of Na/O_2 or Li/O_2 cells, it may happen that oxygen molecules in the electrolyte are consumed much faster than they are supplied to the electrolyte during discharge; thus, severe oxygen deficiency may occur near the electrode. An oxygen-

deficient phase, such as Na_2O_2 or Li_2O, would be generated in such kinetically reducing cases.

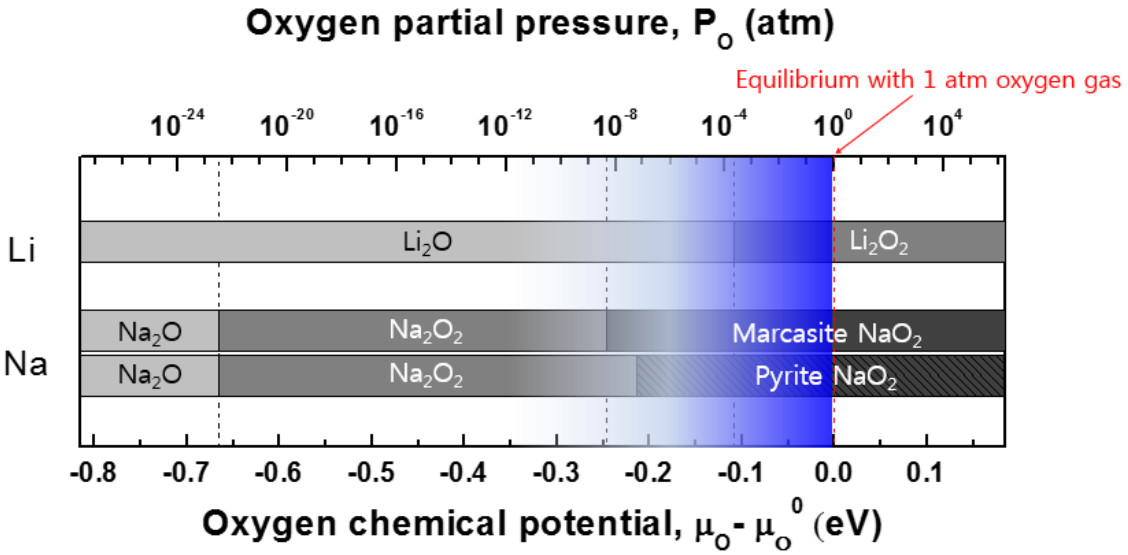

Figure 2. Phase stability map of various lithium/sodium oxides as a function of oxygen chemical potential or oxygen partial pressure. The red line is the oxygen chemical potential where oxygen dissolved in electrolyte is in equilibrium with 1 atm oxygen gas. The blue region is the oxygen chemical potential range under non-equilibrium conditions that can result from fast consumption of O_2 in the electrolyte during discharge.

4.3. The surface energies

4.3.1. Terminations of the surface

The surface energies of the NaO_2, Na_2O_2, and Li_2O_2 were calculated to estimate the equilibrium morphologies of the discharge products and monitor the charging mechanism in the Na/O_2 and Li/O_2 cells. The most stable termination of each surface was selected by calculating all possible terminations for each surface. For example, there are 3 terminations in (100) surface of pyrite NaO_2, designated as O_2(1)-Na(1), O_2(1) and Na(1) in Figure 3(a). The surface energies of each surface are calculated by equation (7) at most reducing condition (equation (12)) and most oxidizing condition (equation (13)). In this case, termination 'O_2(1)-Na(1)' is most stable at both reducing and oxidizing condition as can be seen in table 1. Similar calculations were conducted for all surfaces of pyrite NaO_2, marcasite NaO_2, Na_2O_2, and Li_2O_2. Detailed information of terminations of each surface is provided in Figure 4-6 and Table 2-4.

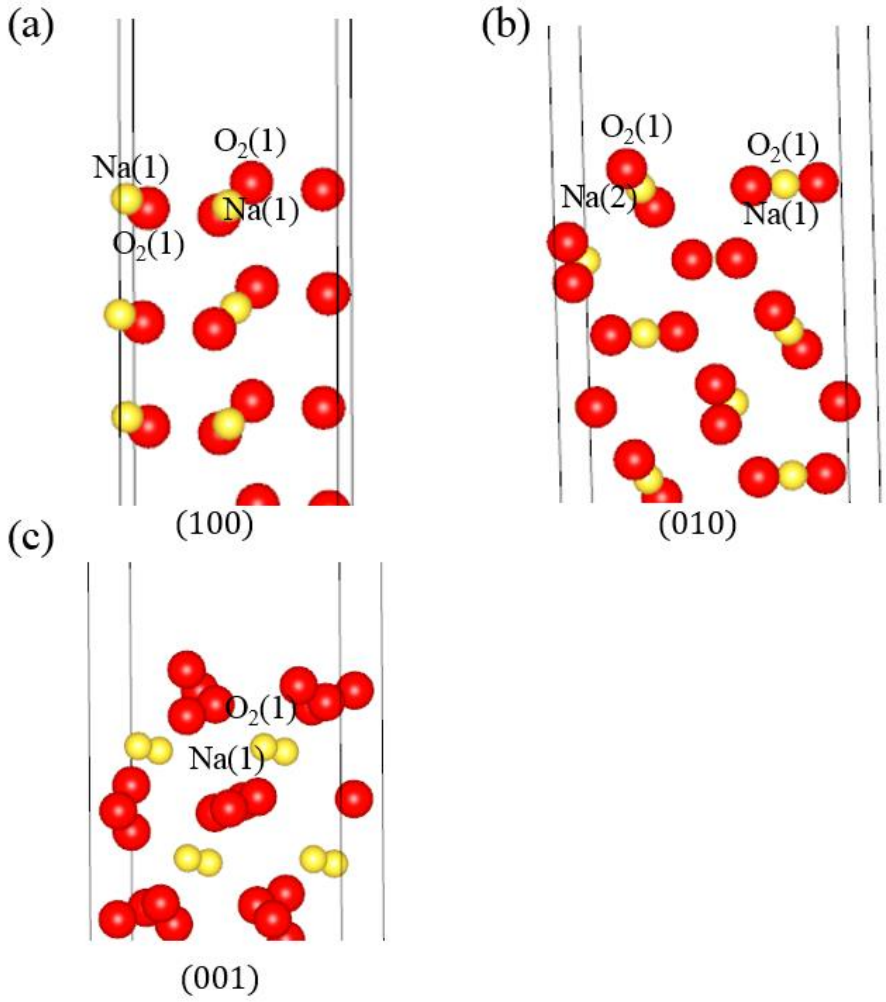

Figure 3. Surface unit cells of pyrite NaO_2. The yellow and red atoms correspond to sodium and oxygen, respectively. Three low-index surfaces were considered. As termination with an O atom rather than an O_2 dumbbell made the surface unstable, such terminations were not considered in this study.

Orientation	Termination	Na_2O_2 limit	O_2 limit
(100)	O_2(1)-Na(1)*	13	13
	O_2(1)	48	21
	Na(1)	128	156
(110)	O_2(1)-Na(1)-Na(2)*	26	26
	O_2(1)	62	42
	Na(1)-Na(2)	51	70
	O_2(1)-Na(1)	28	18
(111)	O_2(1)	34	18
	Na(1)	42	58

Table 1. Surface energies of pyrite NaO_2 for all possible terminations. The star symbols (*) indicate stoichiometric surfaces. The most stable termination of each surface was used to construct the Wulff shape. (in meV/Å ^{2})

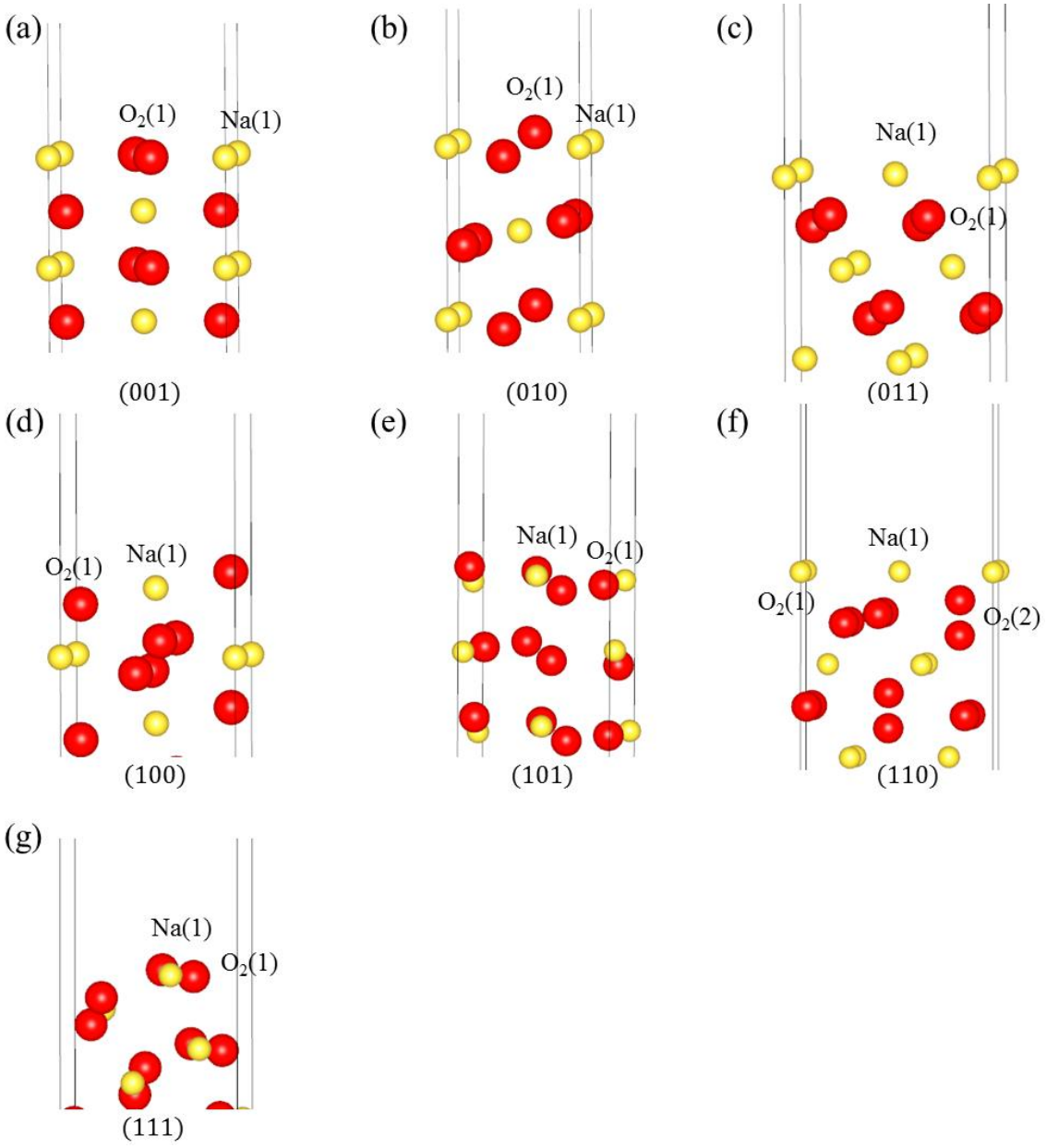

Figure 4. Surface unit cells of marcasite NaO_2. The yellow and red atoms correspond to sodium and oxygen, respectively. Seven low-index surfaces were considered.

Orientation	Termination	Na_2O_2 limit	O_2 limit
(001)	O_2(1)-Na(1)*	29	29
	O_2(1)	35	15
	Na(1)	68	89
(010)	O_2(1)-Na(1)*	23	23
	O_2(1)	52	18
	Na(1)	140	174
(011)	O_2(1)-Na(1)	57	75
	O_2(1)	32	14
(100)	O_2(1)-Na(1)*	37	37
	O_2(1)	49	24
	Na(1)	90	116
(101)	O_2(1)-Na(1)*	16	16
	O_2(1)	47	15
	Na(1)	76	92
(110)	Na(1)-O_2(1)-O_2(2)	65	85
	O_2(1)-O_2(2)	42	21
	O_2(1)*	37	37
	O_2(2)*	37	37
(111)	O_2(1)-Na(1)*	25	25
	O_2(1)	32	17
	Na(1)	52	66

Table 2. Surface energies of NaO_2 for all possible terminations. The star symbols (*) indicate stoichiometric surfaces. (in meV/Å ^{2})

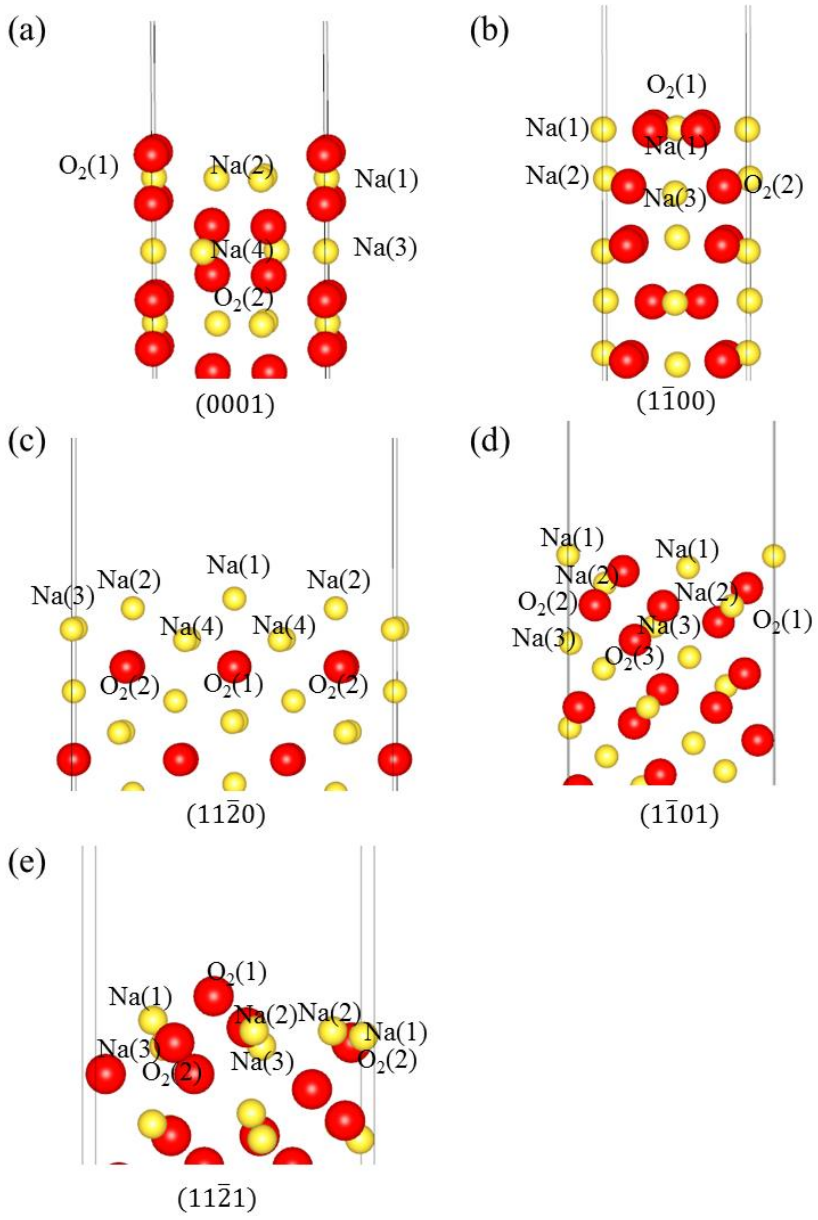

Figure 5. Surface unit cells of Na_2O_2. The yellow and red atoms correspond to sodium and oxygen, respectively. Five low-index surfaces were considered. There were many terminations because of the low symmetry of the Na_2O_2 structure. The top and bottom surfaces of the $(11\bar{2}0)$ and $(11\bar{2}1)$ surfaces could not be terminated equally because of low symmetry, hence atoms that were positioned at the same crystallographic site were terminated.

Orientation	Termination	Na_2O limit	NaO_2 limit
(0001)	O_2(1)-Na(1)-Na(2)-O_2(2)-Na(3)-Na(4)	56	62
	Na(1)-Na(2)-O_2(2)-Na(3)-Na(4)	150	182
	O_2(1)-Na(2)-O_2(2)-Na(3)-Na(4)	43	37
	O_2(1)-Na(1)-O_2(2)-Na(3)-Na(4)	48	29
	O_2(1) -O_2(2)-Na(3)-Na(4)	73	41
	Na(1) -O_2(2)-Na(3)-Na(4)	69	76
	Na(2)-O_2(2)-Na(3)-Na(4)	36	55
	O_2(2)-Na(3)-Na(4)	35	28
	O_2(2)-Na(4)	54	34
	O_2(2)-Na(3)	66	34
	O_2(2)	84	39
$(1\bar{1}00)$	O_2(1)-Na(1)-Na(2)-O_2(2)-Na(3)*	47	47
	Na(1)-Na(2)-O_2(2)-Na(3)	149	180
	O_2(1) -Na(2)-O_2(2)-Na(3)	62	32
	Na(2)-O_2(2)-Na(3)*	51	51
	Na(2)-O_2(2)	49	34
	O_2(2)-Na(3)	50	35
	O_2(2)	63	32
	Na(2)	102	117
$(11\bar{2}0)$	Na(1)-Na(2)-Na(3)-Na(4)-O_2(1)-O_2(2)	136	162
	Na(2)-Na(3)-Na(4)-O_2(1)-O_2(2)	103	120
	Na(3)-Na(4)-O_2(1)-O_2(2)*	32	32
	Na(4)-O_2(1)-O_2(2)	40	31
	O_2(1)-O_2(2)	62	35
	O_2(1)	102	111
	O_2(2)	79	70
$(1\bar{1}01)$	Na(1)-O_2(1)-Na(2)-O_2(2)-Na(3)-O_2(3)	52	57
	O_2(1)-Na(2)-O_2(2)-Na(3)-O_2(3)	41	26
	Na(2)-O_2(2)-Na(3)-O_2(3)	77	82
	O_2(1)-O_2(2)-Na(3)-O_2(3)	73	38
	O_2(1)-Na(2) -Na(3)-O_2(3)	65	70
	O_2(1)-Na(3)-O_2(3)	56	41
	Na(2)-Na(3)-O_2(3)	125	150
	O_2(2)-Na(3)-O_2(3)	75	60
	Na(3)-O_2(3)	77	82
	Na(3)	124	148
	O_2(3)	54	49
$(11\bar{2}1)$	Na(1)-O_2(1)-Na(2)-O_2(2)-Na(3)*	45	45
	O_2(1)-Na(2)-O_2(2)-Na(3)	56	41
	Na(2)-O_2(2)-Na(3)*	76	76
	Na(2)-Na(3)	148	177
	Na(3)	98	112
	O_2(2)-Na(3)	60	46
	O_2(2)	203	174

Table 3. Surface energies of Na_2O_2 for all possible terminations. The star symbols (*) indicate stoichiometric surfaces. (in meV/Å ^{2})

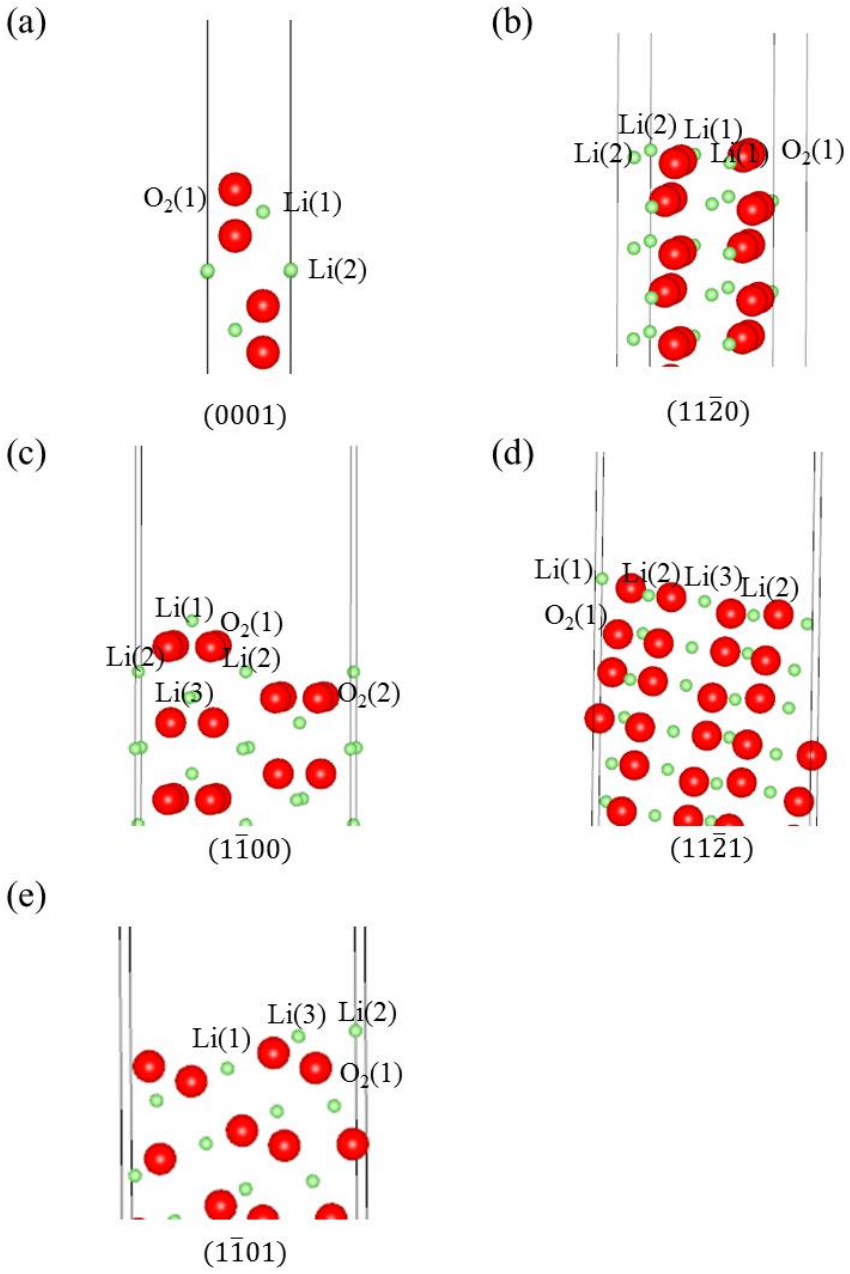

Figure 6. Surface unit cells of Li_2O_2. The green and red atoms correspond to lithium and oxygen, respectively. Five low-index surfaces were considered.

Orientation	Termination	Li_2O limit	O_2 limit
(0001)	O(1)-Li(1)-O(2)-Li(2)	38	32
	Li(1)-O(2)-Li(2)	65	72
	Li(2)	131	138
	O(2)-Li(2)	224	218
$(1\bar{1}00)$	Li(1)-O_2(2)-Li(3)*	35	35
	Li(1)-O_2(1)-Li(2)-O_2(2)-Li(3)	49	45
	O_2(1)-Li(2)-O_2(2)-Li(3)	68	60
	Li(2)-O_2(2)-Li(3)*	119	119
	O_2(2)-Li(3)	42	38
	Li(3)	131	136
$(11\bar{2}0)$	Li(1)-Li(2)-O_2(1)*	55	55
	Li(2)-O_2(1)	47	42
	Li(1)-O_2(1)	49	44
	O_2(1)	52	42
$(1\bar{1}01)$	Li(1)-Li(2)-Li(3)-O_2(1)	78	76
	Li(1)-Li(2)-O_2(1)	84	78
	Li(1)-Li(3)-O_2(1)	91	84
	Li(2)-Li(3)-O_2(1)	102	92
	Li(1)-O_2(1)	93	78
	Li(2)-O_2(1)	107	92
	Li(3)-O_2(1)	95	84
	O_2(1)	94	74
$(11\bar{2}1)$	Li(1)-Li(2)-Li(3)-O_2(1)	56	55
	Li(2)-Li(3)-O_2(1)	48	41
	Li(1)-Li(3)-O_2(1)	54	48
	Li(3)-O_2(1)	56	44

Table 4. Surface energies of Li_2O_2 for all possible terminations. The star symbols (*) indicate stoichiometric surfaces. (in meV/Å ^{2}) The energies of terminations were in good agreement with the results of Mo *et al.*; [Reference 13 in the paper] slight differences derive from computational details. Note that Mo *et al.* referred to the $(11\bar{2}0)$ surface as $(1\bar{1}00)$, $(1\bar{1}00)$ as $(11\bar{2}0)$, $(11\bar{2}1)$ as $(1\bar{1}01)$, and $(1\bar{1}01)$ as $(11\bar{2}1)$. There are no stoichiometric terminations in the $(1\bar{1}01)$ and $(11\bar{2}1)$ surfaces, but Mo *et al.* considered stoichiometric terminations, resulting in different surface energies, for the $(1\bar{1}01)$ and $(11\bar{2}1)$ surfaces.

4.3.2. Wulff construction and equilibrium morphology

The calculated surface energies of NaO_2, Na_2O_2, and Li_2O_2 are summarized in Table 5. The surface energies are shown for both the most oxidizing and reducing conditions because of the possible range of oxygen chemical potential. The surface energy of Li_2O_2 showed a good agreement with the value reported previously,[20] with the slight difference likely due to calculation details and the termination strategy (see the Supplemental Material). Based on the relative surface energies, the equilibrium shapes of NaO_2, Na_2O_2, and Li_2O_2 were estimated using the Wulff construction.[33] Figure 7 shows the predicted shapes of the discharge products under the most oxidizing and reducing conditions. The pyrite NaO_2 particle is mainly composed of (100) surface under reducing conditions (Figure 7(b)), while the shape was truncated by (110) and (111) surfaces in oxidizing conditions (Figure 7(a)). A recent experimental study indicated that the NaO_2 crystallite had a cubic-like morphology (Figure 7(c)) in pyrite phase,[10, 34] corresponding well to our calculated Wulff shape under reducing conditions. It may indicate that the experimental condition of the Na/O_2 cell resembled the oxygen-deficient condition. We expect that the effectively reducing condition can occur when the rate of oxygen consumption in the electrolyte is significantly higher compared to its supply during discharge. Thus, it is also possible that the Na_2O_2 is formed when severely oxygen-deficient environment is imposed under practical experimental conditions. Depending on the surface area of the air electrode and the amount of the electrolyte of the cell, the rate of oxygen consumption and the supply might vary. It is noteworthy that Hartmann et al.,[10] who observed NaO_2 discharge product, used macro gas diffusion layer (GDL) as an air-electrode, while Kim et al.[11] and Liu et al.,[13] who observed Na_2O_2, used high surface area carbon in their air-electrode. The marcasite NaO_2 particle shape was mainly composed of the (010) and (101) surfaces under reducing conditions (Figure 7(e)), and it was truncated by other surfaces, i.e., (011), (001), and (111) under oxidizing conditions (Figure 7(d)). The crystal shape of Na_2O_2 looks more complex and is composed of various surfaces such as (0001), $(11\bar{2}0)$, $(1\bar{1}00)$, and $(1\bar{1}01)$ (Figure 7(f – g)). It contrasts with the shape of Li_2O_2, which was mainly composed of two surfaces; (0001) and $(1\bar{1}00)$ (Figure 7(h – i)). This finding for Li_2O_2 agreed well with other

reports.[29, 35]

Species	Orientation	Most oxidizing condition	Most reducing condition
Pyrite NaO_2	(100)	13.5	13.5
	(110)	26.5	26.5
	(111)	18.4	34.1
Marcasite NaO_2	(001)	14.5	29.4
	(010)	18.3	22.9
	(011)	14.1	31.6
	(100)	23.5	36.8
	(101)	14.5	15.7
	(110)	21.2	36.7
	(111)	16.8	24.7
Na_2O_2	(0001)	28.4	34.6
	$(1\bar{1}00)$	28.7	34.1
	$(1\bar{1}01)$	32.1	42.3
	$(11\bar{2}0)$	30.6	45.8
	$(11\bar{2}1)$	32.1	46.8
Li_2O_2	(0001)	31.7	38.8
	$(1\bar{1}00)$	34.7	34.7
	$(1\bar{1}01)$	78.5	82.8
	$(11\bar{2}0)$	42.0	47.1
	$(11\bar{2}1)$	51.5	54.1

Table 5. Calculated surface energies of the low-index surfaces of pyrite NaO_2, marcasite NaO_2, Na_2O_2, and Li_2O_2 under the most oxidizing and reducing conditions (in meV/Å ^{2}).

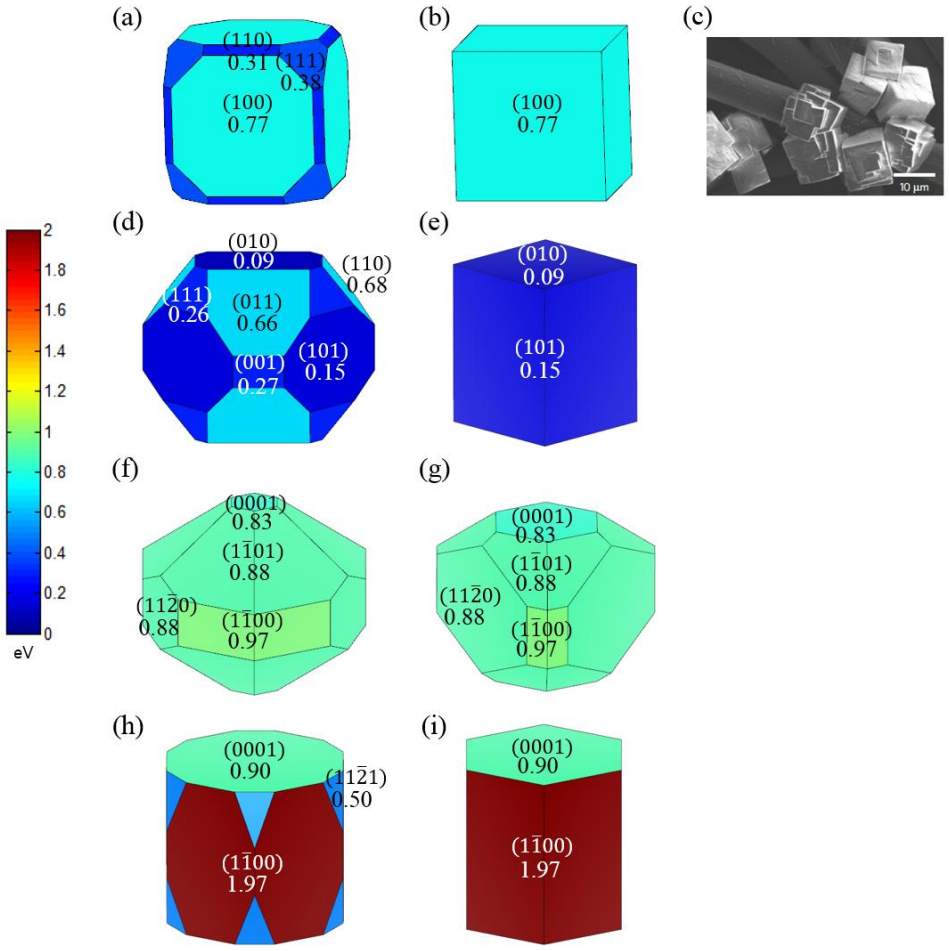

Figure 7. Wulff shapes of (a), (b) pyrite NaO_2, (d), (e) marcasite NaO_2, (f), (g) Na_2O_2, and (h), (i) Li_2O_2 during the OER on the corresponding surfaces. The left sides (a), (d), and (f) are for the most oxidizing conditions, and the right sides (b), (e), and (g) are for the most reducing conditions of each material. (c) SEM image of the pyrite NaO_2 crystallite in the discharged Na/O_2 cell. The calculated energy barrier of OER for all the surfaces are represented as a colored map in the Wulff shape of each material. Major surfaces of the Na discharge products are comprised of the surfaces with low OER barriers. Reproduced with permission from Ref. 14. Copyright 2013 Nature Publishing Group.

4.4. The oxygen evolution reaction mechanism

Given the surface morphologies of the discharge products, we investigated the OER mechanism occurring at the surface. During the OER, oxygen or metal atoms leave the surface upon charging. There are two possible sequences for the decomposition reaction; whether the metal is extracted first or the oxygen molecule evolves first. These steps can be expressed as:

$$M_xO_y \rightarrow M_{x-1}O_y + M^+ + e^- \quad (16)$$

and

$$M_xO_y \rightarrow M_xO_{y-2} + O_2 \quad (17)$$

where M_xO_y is the formula for the surface structures of NaO_2, Na_2O_2, and Li_2O_2, and M represents Na or Li. The energies of the intermediate steps of the OER were considered by removing metal or oxygen molecules from the surface until all the atoms in the surface of the unit cell were consumed. As the final termination is identical to the initial termination when the unit formula is removed from the surface, the entire decomposition procedure could be described by considering one unit cell. Ideally, the OER occurs under the equilibrium potential, $U = 2.41\,V$ for pyrite NaO_2, $U = 2.45\,V$ for marcasite NaO_2, $U = 2.21\,V$ for Na_2O_2, and $U = 2.82\,V$ for Li_2O_2 in equation (15). Due to the unstable intermediate steps during the decomposition, additional potential must be applied to make the reaction occur. Note that the energy barrier calculated here only included a contribution from the unstable chemical intermediate state, while the other effects were neglected. To visualize the total energy barrier required for the reaction, the energy profiles of intermediate steps at each surface were plotted along the reaction coordinate. The energy profiles of the two most stable surfaces of each material are shown in Figure 8. The profiles of other surfaces are provided in Figure 9-12. As shown in Figure 8(a – d), the OER barrier is generally lower for Na/O_2 systems. While the results for Li_2O_2 in Figure 8(g and h) were in good agreement with the previous work,[20] the energy barrier of the NaO_2 decomposition reaction was notably lower for both pyrite and marcasite phases. The energy barrier required to decompose NaO_2 phases were as low as 0.1– 0.8 eV, which contrasts with 0.9 – 2.0 eV for that of Li_2O_2 on major surfaces. Also, the decomposition of Na_2O_2 required 0.8 – 0.9 eV, which is still

lower than that of Li_2O_2 even though it is relatively higher than those of NaO_2. During OER, oxygen removal step significantly affected the total energy barrier (denoted as red steps in the figure) even though these steps were not electrochemical reaction. Moreover, these chemical steps formed substantial barriers in almost all decomposition reactions as shown in Figure 8. It is interesting that it is comparable to well-known water (H_2O) splitting reaction kinetics, where oxygen evolution reaction requires high energy barrier in oxygen bonding formation due to four electrons transfer.[36] Nevertheless, these steps become comparatively smaller in NaO_2 phases than Li_2O_2. We attribute this in part to differences in oxygen contents in each phases. In oxygen-rich NaO_2 phases, the oxygen bonding in the lattice is likely to be weaker than in oxygen-poor Li_2O_2. The strong oxygen bond in the Li_2O_2 crystal lattice causes the O_2-escaping step from the crystal to be less favorable. This is further supported by the less stable chemical step observed for the Na_2O_2 phase than that for NaO_2 phases. Oxygen-poor Na_2O_2 is likely to hold oxygen more strongly in the crystal lattice, leading to a higher energy cost for oxygen evolution. Distinct metal-oxygen bondings in different crystal sites are also partially responsible for different OER barriers. We observed that the volume of prismatic MO_6 was significantly smaller than that of octahedral MO_6 for both the Na and Li phases, with substantially shorter M-O distances. While it is rather counterintuitive since the interstitial volume is generally bigger in prismatic sites than octahedral sites,[37] it indicates that the M-O bond is likely stronger in the prismatic configuration. The higher energy barrier of Na_2O_2 decomposition than that of NaO_2 may be related to the prismatic NaO_6 in Na_2O_2. The stronger binding of Na and oxygen in Na_2O_2 with purely prismatic configuration is expected to be more difficult to break than those in NaO_2 with octahedral configurations. In Li_2O_2, there are both octahedral and prismatic configurations for Li. Since both configurations need to be broken for full decomposition reaction, the rate limiting would occur at prismatic LiO_6. Compact LiO_6 prisms would bind the oxygen strongly, resulting in a high energy barrier for decomposition. It is worthwhile to note that the low overpotential was observed for the NaO_2 decomposition reaction by Hartmann et al.,[10] while relatively higher overpotential was experimentally observed for that of Na_2O_2.[13]

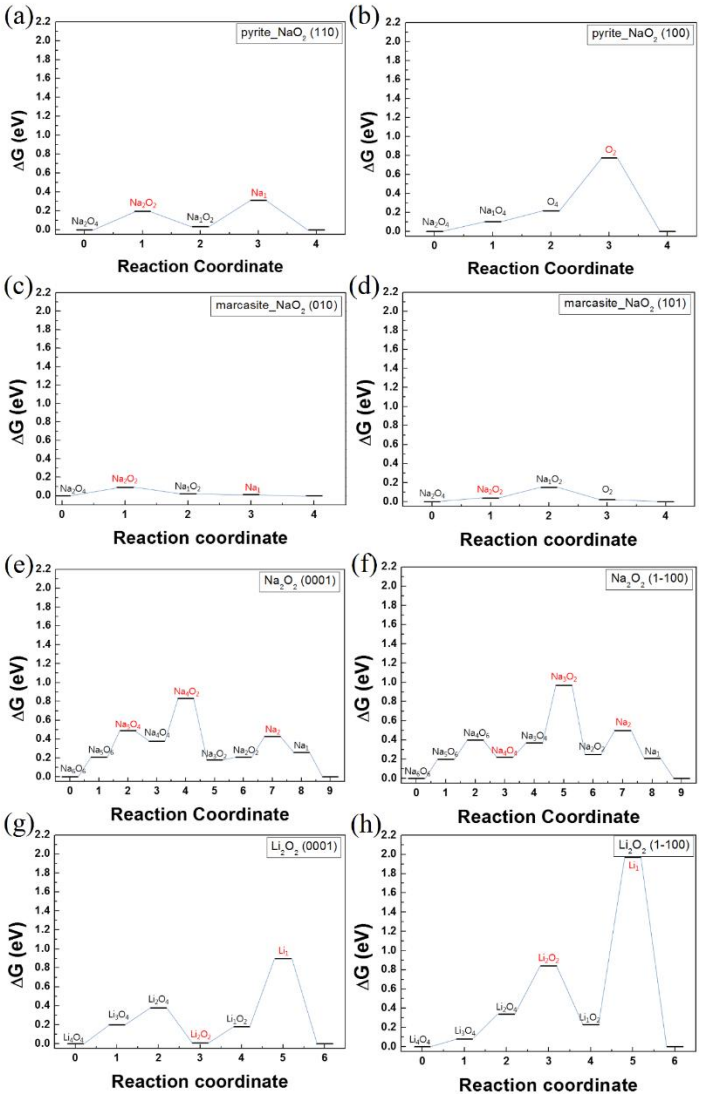

Figure 8. OER energy profile of the surfaces in pyrite NaO_2, marcasite NaO_2, Na_2O_2, and Li_2O_2. The surfaces of interest were selected: (a) (110) surface of pyrite NaO_2, (b) (100) surface of pyrite NaO_2, (c) (101) surface of marcasite NaO_2, (d) (010) surface of marcasite NaO_2, (e) (0001) surface of Na_2O_2, (f) $(1\bar{1}00)$ surface of Na_2O_2, (g) (0001) surface of Li_2O_2, and (h) $(1\bar{1}00)$ surface of Li_2O_2. The most favorable reaction paths are shown. The chemical steps are shown in red.

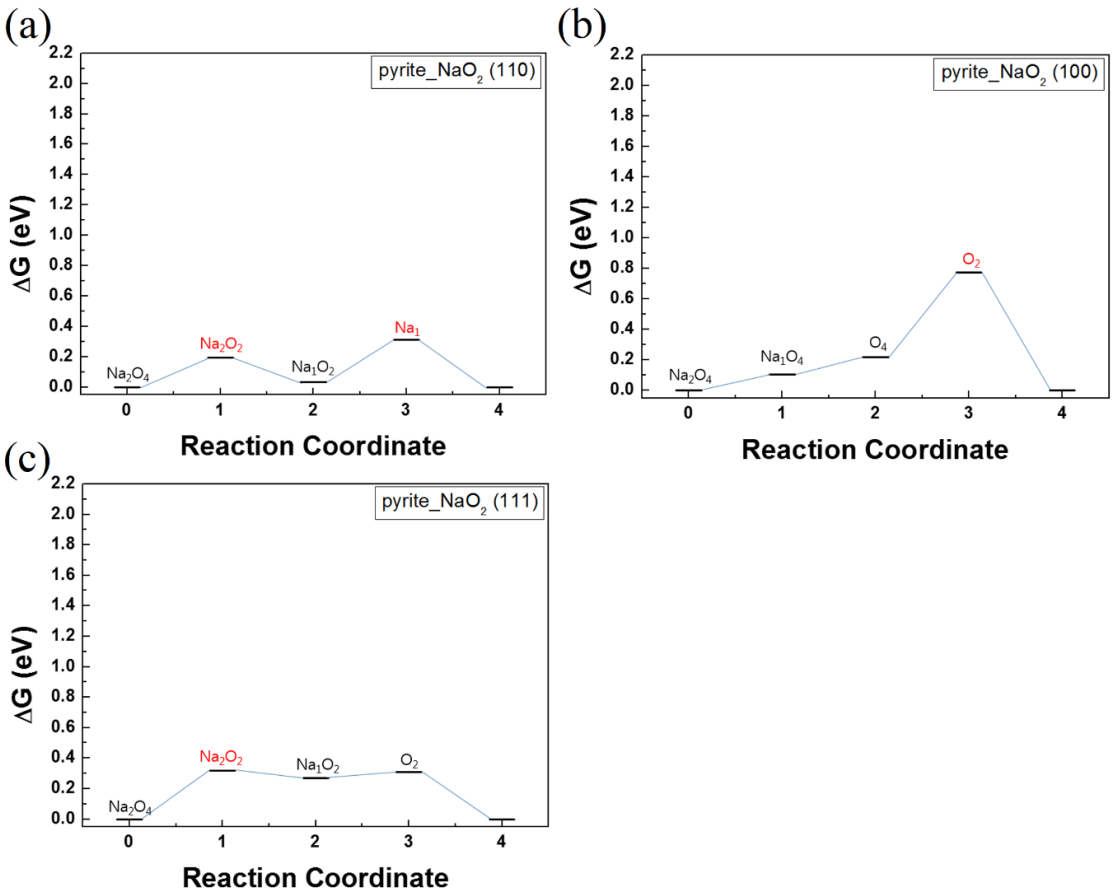

Figure 9. The OER energy profile for pyrite NaO_2. (a) (100) surface of pyrite NaO_2, (b) (110) surface of pyrite NaO_2, (c) (111) surface of pyrite NaO_2. The most favorable reaction paths are shown. The chemical steps are shown in red.

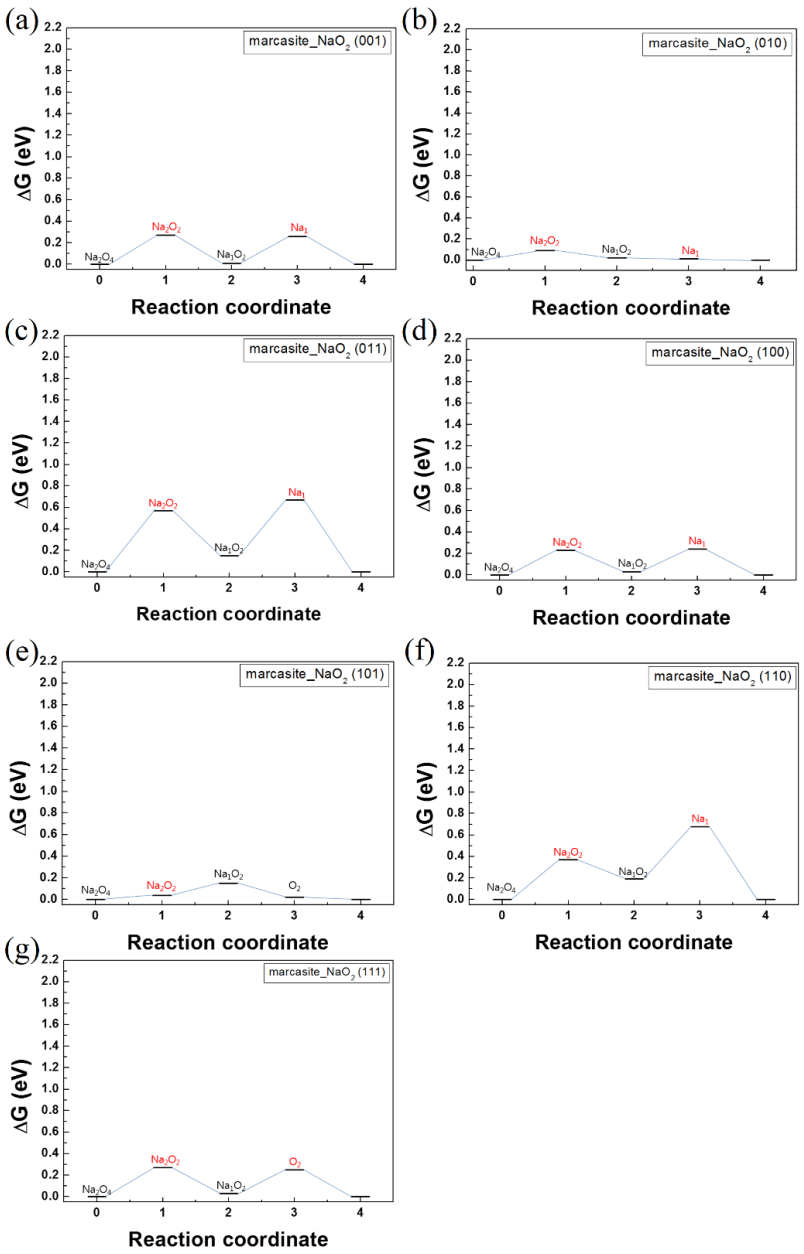

Figure 10. The OER energy profile for marcasite NaO_2. (a) (001) surface of marcasite NaO_2, (b) (010) surface of marcasite NaO_2, (c) (011) surface of marcasite NaO_2, (d) (100) surface of marcasite NaO_2, (e) (101) surface of marcasite NaO_2, (f) (110) surface of marcasite NaO_2, and (g) (111) surface of marcasite NaO_2. The most favorable reaction paths are shown. The chemical steps are shown in red.

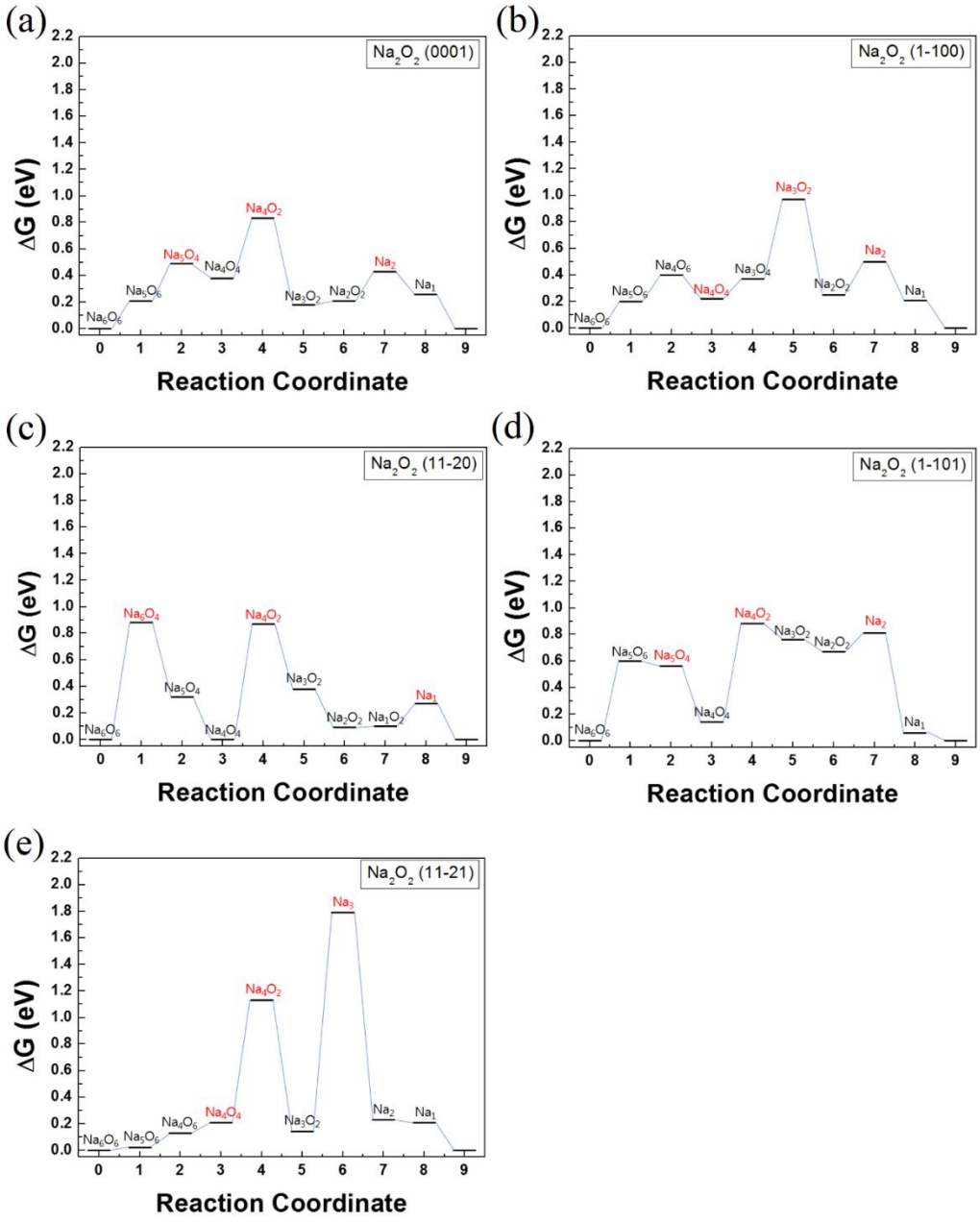

Figure 11. The OER energy profile for Na_2O_2. (a) The (0001) surface of Na_2O_2, (b) the $(1\bar{1}00)$ surface of Na_2O_2, (c) the $(11\bar{2}0)$ surface of Na_2O_2, (d) the $(1\bar{1}01)$ surface of Na_2O_2, and (e) the $(11\bar{2}1)$ surface of Na_2O_2. The most favorable reaction paths are shown. The chemical steps are shown in red.

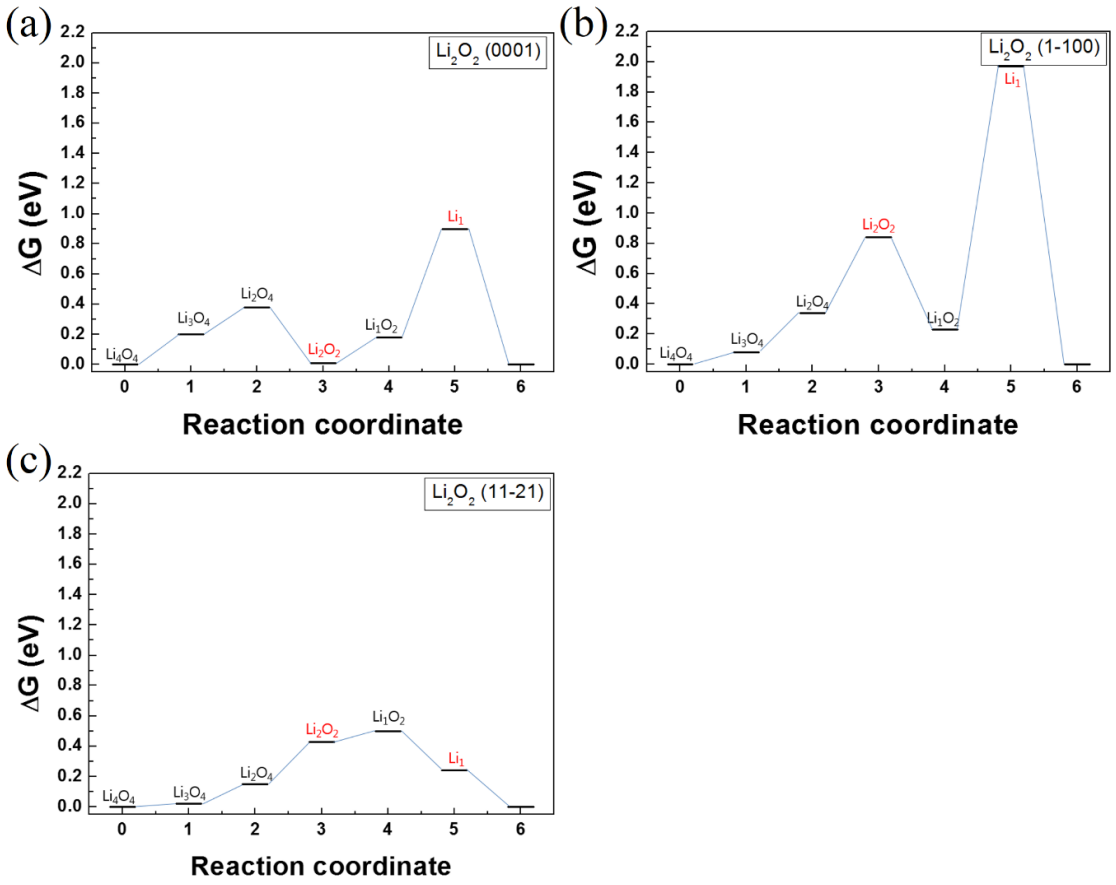

Figure 12. The OER energy profile for Li_2O_2. (a) (0001) surface of Li_2O_2, (b) $(1\bar{1}00)$ surface of Li_2O_2, and (c) $(11\bar{2}1)$ surface of Li_2O_2. The most favorable reaction paths are shown. The chemical steps are shown in red. Since $(11\bar{2}0)$ and $(1\bar{1}01)$ surfaces cannot be found in Wulff shape, the OER profiles of these surfaces were not calculated.

4.5. Electronic conductivity of discharge product

Electrical conductivities of discharge products may influence the overall overpotential of Na/O_2 cell and Li/O_2 cell in addition to the energy barrier for OER. Many groups[38-40] studied the charge transport mechanism and the conductivity of Li_2O_2 and suspected that poor conductivity of Li_2O_2 can be culprit for high overpotential in Li/O_2 cell. In this respect, we compared bandgaps of discharge products by HSE06 hybrid functional calculation. Bandgaps of pyrite NaO_2, marcasite NaO_2, Na_2O_2 and Li_2O_2 were found to be 1.09 eV, 1.11 eV, 2.94 eV, and 4.60 eV, respectively, from the density of states for each materials (Figure 13). We found that bandgaps of sodium phases are generally lower than Li_2O_2 possibly resulting in better electronic conductivity. However, the bandgaps are still too high to account for the exceptionally low overpotential of Na/O_2 cells, even though the electronic structure of off-stoichiometric products such as $NaO_{2-\delta}$ and $Na_{1-\delta}O_2$ should be investigated further to confirm this.

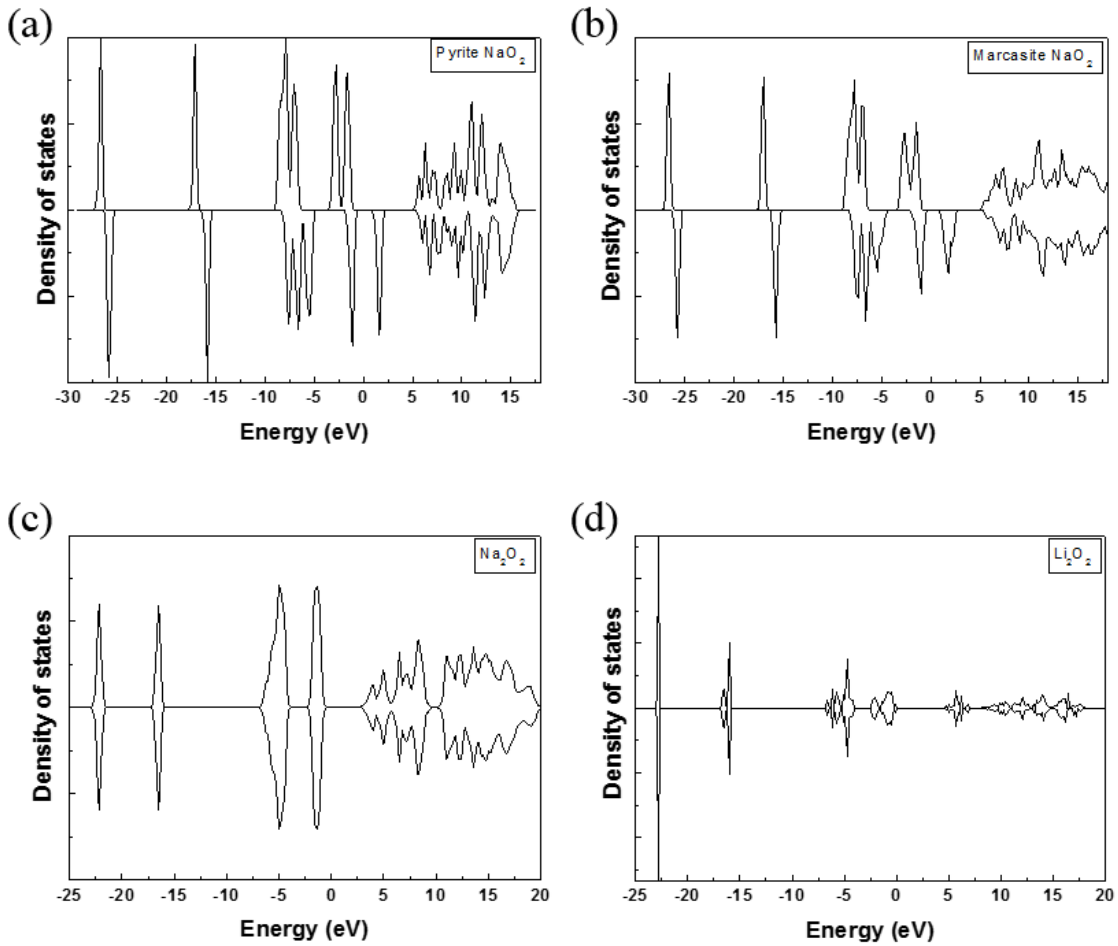

Figure 13. Density of state of (a) pyrite NaO_2, (b) marcasite NaO_2, (c) Na_2O_2, (d) Li_2O_2.

Chapter 5. Conclusion

The reaction mechanism in Na/O_2 cell was investigated using first-principles calculations and compared with that of Li/O_2 cell. We found that the discharge products of the Na/O_2 and Li/O_2 cells are NaO_2 and Li_2O_2, respectively in standard conditions, even though it can vary depending on the effective atmosphere in the experiment. Surface calculations of discharge phases revealed the equilibrium shapes of the particles, which are in an excellent agreement with the experimental observation. Furthermore, the simulation of OERs on major surfaces of discharge products indicated that the NaO_2 decomposition reaction required less energy barrier than those of Li_2O_2 decomposition providing a hint for a low overpotential of Na/O_2 cell compared to Li/O_2 cell. [41]

Reference

1. Abraham, K. M.; Jiang, Z., *J. Electrochem. Soc.* **1996,** 143, (1), 1-5.

2. Freunberger, S. A.; Chen, Y.; Drewett, N. E.; Hardwick, L. J.; Bardé, F.; Bruce, P. G., *Angew. Chem. Int. Ed.* **2011,** 50, (37), 8609-8613.

3. Débart, A.; Bao, J.; Armstrong, G.; Bruce, P. G., *J. Power Sources* **2007,** 174, (2), 1177-1182.

4. Débart, A.; Paterson, A. J.; Bao, J.; Bruce, P. G., *Angew. Chem.* **2008,** 120, (24), 4597-4600.

5. Bruce, P. G.; Freunberger, S. A.; Hardwick, L. J.; Tarascon, J.-M., *Nat. Mater.* **2012,** 11, (1), 19-29.

6. Girishkumar, G.; McCloskey, B.; Luntz, A. C.; Swanson, S.; Wilcke, W., *J. Phys. Chem. Lett.* **2010,** 1, (14), 2193-2203.

7. Ottakam Thotiyl, M. M.; Freunberger, S. A.; Peng, Z.; Bruce, P. G., *J. Am. Chem. Soc.* **2012,** 135, (1), 494-500.

8. Lim, H.-D.; Park, K.-Y.; Gwon, H.; Hong, J.; Kim, H.; Kang, K., *Chem. Commun.* **2012,** 48, (67), 8374-8376.

9. Peng, Z.; Freunberger, S. A.; Chen, Y.; Bruce, P. G., *Science* **2012,** 337, (6094), 563-566.

10. Hartmann, P.; Bender, C. L.; Vračar, M.; Dürr, A. K.; Garsuch, A.; Janek, J.; Adelhelm, P., *Nat. Mater.* **2013,** 12, (3), 228-232.

11. Kim, J.; Lim, H.-D.; Gwon, H.; Kang, K., *Phys. Chem. Chem. Phys.* **2013,** 15, (10), 3623-3629.

12. Peled, E.; Golodnitsky, D.; Mazor, H.; Goor, M.; Avshalomov, S., *J. Power Sources* **2011,** 196, (16), 6835-6840.

13. Liu, W.; Sun, Q.; Yang, Y.; Xie, J.-Y.; Fu, Z.-W., *Chem. Commun.* **2013,** 49, (19), 1951-1953.

14. Kresse, G.; Furthmüller, J., *Phys. Rev. B* **1996,** 54, (16), 11169-11186.

15. Seo, D.-H.; Gwon, H.; Kim, S.-W.; Kim, J.; Kang, K., *Chem. Mater.* **2009,** 22, (2), 518-523.

16. Seo, D.-H.; Kim, H.; Park, I.; Hong, J.; Kang, K., *Phys. Rev. B* **2011,** 84, (22), 220106.

17. Blöchl, P. E., *Phys. Rev. B* **1994,** 50, (24), 17953-17979.

18. Seo, D.-H.; Kim, H.; Kim, H.; Goddard, W. A.; Kang, K., *Energy Environ. Sci.* **2011,** 4, (12), 4938-4941.

19. Seo, D.-H.; Park, Y.-U.; Kim, S.-W.; Park, I.; Shakoor, R. A.; Kang, K., *Phys. Rev. B* **2011,** 83, (20), 205127.

20. Mo, Y.; Ong, S. P.; Ceder, G., *Phys. Rev. B* **2011,** 84, (20), 205446.

21. Kramer, D.; Ceder, G., *Chem. Mater.* **2009,** 21, (16), 3799-3809.

22. Ramamoorthy, M.; Vanderbilt, D.; King-Smith, R. D., *Phys. Rev. B* **1994,** 49, (23), 16721-16727.

23. Christensen, A.; Carter, E. A., *Phys. Rev. B* **1998,** 58, (12), 8050-8064.

24. Wang, X.-G.; Chaka, A.; Scheffler, M., *Phys. Rev. Lett.* **2000,** 84, (16), 3650-3653.

25. Reuter, K.; Scheffler, M., *Phys. Rev. Lett.* **2003,** 90, (4), 046103.

26. Wang, L.; Zhou, F.; Ceder, G., *Electrochem. Solid-State Lett.* **2008,** 11, (6), A94-A96.

27. Reuter, K.; Scheffler, M., *Phys. Rev. B* **2001,** 65, (3), 035406.

28. Wang, L.; Maxisch, T.; Ceder, G., *Phys. Rev. B* **2006,** 73, (19), 195107.

29. Radin, M. D.; Rodriguez, J. F.; Tian, F.; Siegel, D. J., *J. Am. Chem. Soc.* **2011,** 134, (2), 1093-1103.

30. Hummelshoj, J. S.; Blomqvist, J.; Datta, S.; Vegge, T.; Rossmeisl, J.; Thygesen, K. S.; Luntz, A. C.; Jacobsen, K. W.; Norskov, J. K., *J. Chem. Phys.* **2010,** 132, (7), 071101-4.

31. Hummelshoj, J. S.; Luntz, A. C.; Norskov, J. K., *J. Chem. Phys.* **2013,** 138, (3), 034703-12.

32. Attema, J. J.; de Wijs, G. A.; Blake, G. R.; de Groot, R. A., *J. Am. Chem. Soc.* **2005,** 127,

(46), 16325-16328.

33. Wulff, G., *Z Krystallogr. Mineral.* **1901,** 34, 449.

34. Hartmann, P.; Bender, C. L.; Sann, J.; Durr, A. K.; Jansen, M.; Janek, J.; Adelhelm, P., *Phys. Chem. Chem. Phys.* **2013**.

35. Nicola, S., *Nanotechnology* **2009,** 20, (44), 445703.

36. Bediako, D. K.; Surendranath, Y.; Nocera, D. G., *J. Am. Chem. Soc.* **2013,** 135, (9), 3662-3674.

37. Callister, W. D., *Materials Science and Engineering: An Introduction*. 8th ed.; Wiley: 2009; p 992.

38. Ong, S. P.; Mo, Y.; Ceder, G., *Phys. Rev. B* **2012,** 85, (8), 081105.

39. Radin, M. D.; Siegel, D. J., *Energy Environ. Sci.* **2013,** 6, (8), 2370-2379.

40. Garcia-Lastra, J. M.; Myrdal, J. S. G.; Christensen, R.; Thygesen, K. S.; Vegge, T., *J. Phys. Chem. C* **2013,** 117, (11), 5568-5577.

41. Lee, B.; Seo, D.-H.; Lim, H.-D.; Park, I.; Park, K.-Y.; Kim, J.; Kang, K., *Chem. Mater.* **2014**.

국문요약

리튬-공기 전지는 지금까지 보고된 전지 시스템 중 가장 높은 이론용량과 에너지밀도를 가지고 있어 활발하게 연구되고 있다. 하지만, 리튬-공기 전지 시스템은 사이클 특성이 나쁜 점과 높은 충전 과전압으로 인해 에너지 효율이 낮은 점이 가장 큰 단점으로 지적되고 있다. 그런데 최근에 낮은 충전 과전압을 가지며 높은 에너지 효율을 보이는 새로운 금속-공기 전지 시스템인 소듐-공기 전지가 보고되었는데, 이는 소듐-공기 전지가 리튬-공기 전지 시스템과 비슷한 거동을 보일 것이라는 예상을 깬 우수한 결과이다. 이것은 두 시스템에 근본적으로 다른 키네틱이 작용하고 있음을 암시한다. 따라서 본 연구에서는 소듐-공기 전지 셀에서의 반응 메커니즘을 제일원리 계산을 통해 알아보았다. 리튬-공기전지와의 비교 분석을 위해 소듐-공기 전지와 리튬-공기 전지의 가능한 반응생성물들에 대한 상평형도를 그렸고 이를 통해 다른 구동 환경에서 어떤 상이 생성되는지를 설명하였다. 가능한 반응생성물인 NaO_2, Na_2O_2, Li_2O_2의 주된 표면에서 일어나는 산소발생반응에 대해 계산한 결과, NaO_2가 분해되는 반응의 활성화 에너지가 Li_2O_2의 그것보다 확연히 낮음을 확인하여 소듐-공기 전지의 낮은 과전압의 원인을 밝힐 수 있었다.

주요어 : 금속-공기 전지, 소듐-공기 전지, 제일원리계산, 과전압, 산소발생반응

학 번 : 2012-20622

감사의 글

가장 먼저 부족한 저를 이끌어 주시고 믿어 주시는 강기석 교수님께 감사의 말씀을 올리고 싶습니다. 지금껏 지낸 날보다 앞으로 지낼 날이 더 많음을 알기에 앞으로도 좋은 가르침과 말씀들 부탁드립니다. 그리고 교수님의 믿음과 기대에 부응하는 명예로운 제자가 되기 위해 열심히 노력하겠습니다. 다음으로 제가 이 자리에 있게 해 주신 사랑하는 가족들, 아버지(이소영), 어머니(박석란), 누나(이유진) 모두 감사합니다. 힘든 일이나 어려운 일이 집에 많았을 텐데 저에게 내색 하나 하지 않으시고 제가 공부에만 집중할 수 있도록 해 주셨기 때문에 제가 이렇게 당당히 석사졸업을 할 수 있었던 것 같습니다. 앞으로도 모두 건강하고 행복했으면 좋겠습니다. 그리고 저를 항상 응원해 주시는 일가 친척분들께도 감사드립니다. 또한 항상 저를 이끌어 주시고 힘이 되어 주는 실험실 선배님들과 동기들, 후배들에게 진심으로 감사를 표합니다. 먼저 가장 많이 조언을 해 주셨고 후배들에게도 항상 따뜻하게 대해 주신 동화형, 항상 감사드리고 존경합니다. 지금은 미국에 나가 계시지만 꼭 감사의 말씀 전해드리고 싶습니다. 또 운동도 잘하시고 연구도 잘하시는 포스닥 영수형, 앞으로도 같이 재미있는 연구 많이 했으면 좋겠습니다. 그리고 차갑게 대하시는 것 같지만 저희를 항상 생각해 주시는 혁조형, 항상 지나고 보면 형의 말씀은 옳았던 것 같아요. 앞으로도 말 잘 듣겠습니다. 또 언제나 분위기를 띄워주시고 제가 심심해 보일 때 말 걸어 주시는 종순이형, 항상 감사드립니다. 저랑 같이 소듐-에어 연구하시는 진수형, 같이 디스커션하면서 많은 아이디어 얻고 있어요. 앞으로 같이 좋은 연구 많이 하면 좋겠습니다. 그리고 항상 제 편에서 말을 들어 주시는 영욱이형, 힘든 시절에 힘이 많이 되었어요. 앞으로도 많은 덕담(?) 부탁드립니다. 놀 때도 재미있게 놀고, 연구도 재미있게 하시는 지현이형, 긍정적인 파워를 많이 받아가고 있어요. 감사합니다. 자주 뵙지는 않지만 항상 푸근하신 정근이형, 앞으로 많이 뵙고 싶어요. 또 저희에게 많은 조언 해주시는 해겸이형, 항상 말 잘 새겨듣고 있습니다. 또 공부를 즐기시고 꼼꼼하게 연구하시는 규영이형, 거기다 유머러스하시기까지 하셔서 본받고 싶어요. 자기주장이 확실하시고 행동력이 강하신 현 계산팀 치프 인철이형, 앞으로도 계산정권(?) 잘

부탁드립니다. 항상 즐거운 술자리를 만들어 주시는 형섭이형, 저희에게 시켜도 될 일을 많이 도와주시거나 도맡아 하시고 하셔서 죄송하고 감사합니다. 연구도 노는 것도 항상 성실하고 최선을 다하시는 희대형, 연구나 생활하는데 있어 크고 작은 조언들이 정말 많은 도움이 되었어요. 또한 저와 희로애락을 같이한(?) 동기 성균이, 인경이, 영준이, 가르쳐 줄 것보다 제가 배울게 더 많은 후배들 교진이, 현아, 갑인이, 인상이, 모두 고맙고 앞으로 같이 많이 발전해 나갔으면 좋겠습니다. 그리고 서울대 재료과 동기들, 특히 소중한 친구들 재민이, 현이, 기동이, 재훈이, 재욱이형에게 감사를 드리고, 많은 추억 함께 했던 동아리 선배님들과 친구들과 후배들, 홍재형, 희현누나, 도경이형, 규근이, 제욱이, 민규형, 수미, 영선이, 세미, 송이, 순현이, 동석이, 신우, 유림이, 수진이, 나리, 종하, 태우, 진이, 수영이, 소현이, … 등등 많은 분들께도 감사를 드립니다. 마지막으로 자주는 못 보지만 볼 때마다 힘을 주는 고향 친구들, 성훈이, 기문이, 찬희, 진형이, 성헌이, 민구, 상준이, 회훈이, 주성이에게 감사를 표합니다.